MASTER THESIS

Thesis submitted in partial fulfillment of the requirements for the degree of Master of Science in Engineering at the University of Applied Sciences Technikum Wien - Degree Program Tissue Engineering and Regenerative Medicine

Injectable Shear-Thinning Hydrogel Composed of Silicate Nanoplatelets and Gelatin with Growth Factor Encapsulated Polycaprolactone Particles and Cells

By: Sobha Karuthedom George, Bsc
Student Number: 1510692022

Cambridge, Massachusetts, 01.09.2017

FH University of Applied Sciences TECHNIKUM WIEN

Declaration of Authenticity

“As author and creator of this work to hand, I confirm with my signature knowledge of the relevant copyright regulations governed by higher education acts (for example see §§ 21, 42f and 57 UrhG (Austrian copyright law) as amended as well as § 14 of the Statute on Studies Act Provisions / Examination Regulations of the UAS Technikum Wien).

In particular I declare that I have made use of third-party content correctly, regardless what form it may have and I am aware of any consequences I may face on the part of the degree program director if there should be evidence of missing autonomy and independence or evidence of any intent to fraudulently achieve a pass mark for this work (see § 14 para. 1 Statute on Studies Act Provisions / Examination Regulations of the UAS Technikum Wien).

I further declare that up to this date I have not published the work to hand nor have I presented it to another examination board in the same or similar form. I affirm that the version submitted matches the version in the upload tool.”

Cambridge MA, 01.09.2017

Place, Date

Signature

Abstract

Repair of larger size bone defects are restricted due to inadequate vascularization and impaired bone regeneration. Bone grafts are vital for treating many conditions that cause immense global burden. Although bone possesses remarkable self-healing and regenerative potential, there are many clinical cases in which the size, location and surrounding environment of the bone defect can lead to improper healing. Despite the high innate capacity of bone, effective bone regeneration involves an intricate and orchestrated cascade of growth factors and cells that play a pivotal role. The objective of this work was to develop an ideal shear-thinning nanocomposite hydrogel that was made of synthetic silicate nanoplatelets and the protein gelatin. The nanocomposite was designed to have a patterned structure consisting of a bone part with osteoblast cells and a vessel part with mouse endothelial cells and vascular endothelial growth factor (VEGF) loaded polycaprolactone nanoparticles. This study also investigated the effect of slow release of VEGF on the growth and proliferation of cells encapsulated in the hydrogel. Mechanical tests showed that the scaffold can be easily injected through catheters and needles. The gel demonstrated good mechanical strength and stability during injectability and rheology measurements. The gel demonstrated rheological characteristics of a shear-thinning material and could rapidly flow under stress and solidify once stress was relieved. The *in vitro* biocompatibility of the gel was examined by culturing endothelial cells and osteoblasts in the gel for 7 days. The results show that the gel can support cell growth and the addition of VEGF loaded particles helped further enhance the expansion of the vascular cells. On day 7 of culture, co-culture showed a 14.8% higher proliferation with the addition of VEGF loaded particles. The gel demonstrated its potential to be easily printed using a customized multi-material bioprinting device. The results of this thesis, shows that the injectable shear-thinning hydrogel has the potential to be used as a vascularized bone scaffold material. The gel represents a promising tool that can change the current clinical practice for treating non-union defects and could significantly improve bone healing. The further exploration of this scaffold material can help scientific knowledge in the field of skeletal tissue engineering by examining synergistic cross-talk between bone cells and vascular cells during bone regeneration at the defect site.

Keywords: Osteogenesis, Angiogenesis, Bone Tissue Engineering, Shear-Thinning Biomaterials, Polycaprolactone, VEGF

Acknowledgements

Firstly, I would like to express my sincere gratitude to Prof. Ali Khademhosseini for giving me the opportunity to work in his lab and for providing the means for this project. I would also like to thank the Austrian Marshall Plan Foundation for the financial support that made my internship in the US possible.

Further, I would like to thank my university supervisor, Anna Weihs, who offered her continuous advice and encouragement throughout the course of writing this thesis. I am very thankful for her guidance and support throughout this thesis. A special thanks to Dr. Hae Lin Jang for giving me the opportunity to be a part of her subgroup. I highly appreciate the continuous support, patience, motivation and guidance she gave me throughout my internship. I could not have imagined having a better supervisor. By encouraging us to work as a team, she truly helped create a friendly and productive working environment.

A very specially thank you to Emine Alarçin who has been more than a supervisor. I am thankful for her kindness and support, but most importantly for her friendship. I have learned a lot from her and consider myself extremely lucky to have had the opportunity to have got to know her and work with her, as she is truly a wonderful person.

I would also like to thank all the members of the nanotechnology subgroup for the friendly work environment and for their guidance and advice. Special thanks to Denata Syla, Jin Zhang, Tae Yong Lee, Meadhbh Brennan, Wei Zhu and Dong Hoon Lee for all their help throughout the course of my internship, for motivating me and for all the fun moments we shared. Finally, I would like to thank my family for always encouraging me and for their constant support, both financially and emotionally. I owe them all that I am today and am very lucky to have them in my life.

Table of Contents

1 Introduction

The worldwide occurrence of bone ailments are steadily increasing and will probably double by 2020, particularly in the aging populations. Globally, around 2 million bone implant surgeries are performed yearly, with 500,000 surgeries performed in the united states. After blood transfusion, bone implants are the next most transplanted tissue in the world [1, 2]. It is estimated that one out of three people suffer from bone fracture during their life span. Large bone defects can be caused by degenerative pathological condition or external trauma. The field of bone tissue engineering has realized great progress in the past years. However, the strategies to overcome larger bone defects remains a problem [3-6]. Around 5 - 10% of all fracture cases are estimated to be non-union fractures. This occurs if the size of the bone damage is much greater than the critical size, due to which the bone cannot heal spontaneously. To treat such fractures, clinical intervention and tissue engineered bone scaffolds are required. These fractures cause a lot of pain and discomfort to the patients and cause great economic burden [3-8]. The patient will suffer severe disabilities, as the natural healing process of the broken bone is unable to completely heal the fracture. If the defect size is small, then the body's own repair mechanism can initiate an endogenous healing process. During this, many cells, such as inflammatory cells, mesenchymal stem cells (MSCs) and osteogenic cells come together and work to heal the damaged bone. This can result in a nearly scar less healing [9], which leads to the formation of new bone tissue with the same mechanical and physiochemical properties as the surrounding native tissue [10, 11].

Bone is important for many vital functions of the body including the maintenance of structure, movement, protection of organs, among others [12, 13]. Thus, the tissue engineered bone scaffold should possess the capability to heal large non-union bone defects by linking the broken bone parts and filling any void space. The scaffold should allow proper vascularization to the surrounding tissue and supply adequate amounts of cells, oxygen and nutrients [9]. These bone scaffolds can be either synthetic, inorganic, or combinations of biological organics and can be used instead of autogenous or allogenous bone grafts for treating bone defects [14]. An ideal bone scaffold would mimic the native bone tissue and provide a matrix wherein the bone cells can grow and differentiate further. The osteoconductive matrix should promote vascularization and deliver osteoinductive factors to promote bone formation [15]. The use of insufficient bone scaffolds for treatment of large bone defects can lead to avascular necrosis, which can cause destruction of the bone tissue. Bones of the body that have better stability and blood circulation, such as the toe bone, have low risk of developing a non-union after a fracture [16, 17]. On the other hand, bones that have limited blood supply, such as the neck, femoral head and wrist bone, are at high risk of

developing a non-union after a fracture [16-18]. However, despite recent advances in orthopedics research, complete treatment of non-union fracture still remains a long-standing challenge. Most current bone implants have limited integration with surrounding tissues, which is mainly contributed by poor linkage to the vascular system of the host [19-23]. Most bone implant materials today are restricted to inorganic bone materials and do not give enough focus to vascularization of the bone tissue [3-6]. These implants are still not sufficient for generating vascularized bone tissue and often exhibit impaired healing [24-26]. In this respect, there is a need to develop new and improved bone implants that can promote blood vessel formation throughout the scaffold and promote rapid regeneration.

1.1 Architecture of bone and the bone vascular system

Bone tissue comprises of a peripheral layer, called cortical bone and an inner layer, that is called spongy bone (see Figure 1). Around 80% of the total bone mass in an adult human is made up of the cortical bone. The cortical bone is very dense and has low porosity of around 20% and high mechanical strength of around 150 MPa. On the other hand, the cancellous bone makes up 20% of the total bone mass and has about 50% porosity. The cancellous bone, when compared to the cortical bone, only has about 10% mechanical strength. Osteons are small functional units inside the cortical bone part [27]. They comprise of the central Haversian canals, that have nerves and blood vessels in them. On the other hand, the cancellous bone does not have any osteon units. Both cortical and cancellous layers both contain of a well vascularized system within them. The existence of a vascular network is important in order to supply nutrients and for the removal of waste products [24, 27]. When damage occurs in bone, angiogenesis and osteogenesis occur in a coupled manner, where blood vessels play an important role [25] in supporting the growth and activity of osteogenic cells [28]. On the other hand, alternations to the bone vasculature can reduce bone growth and lead to skeletal diseases [29-32].

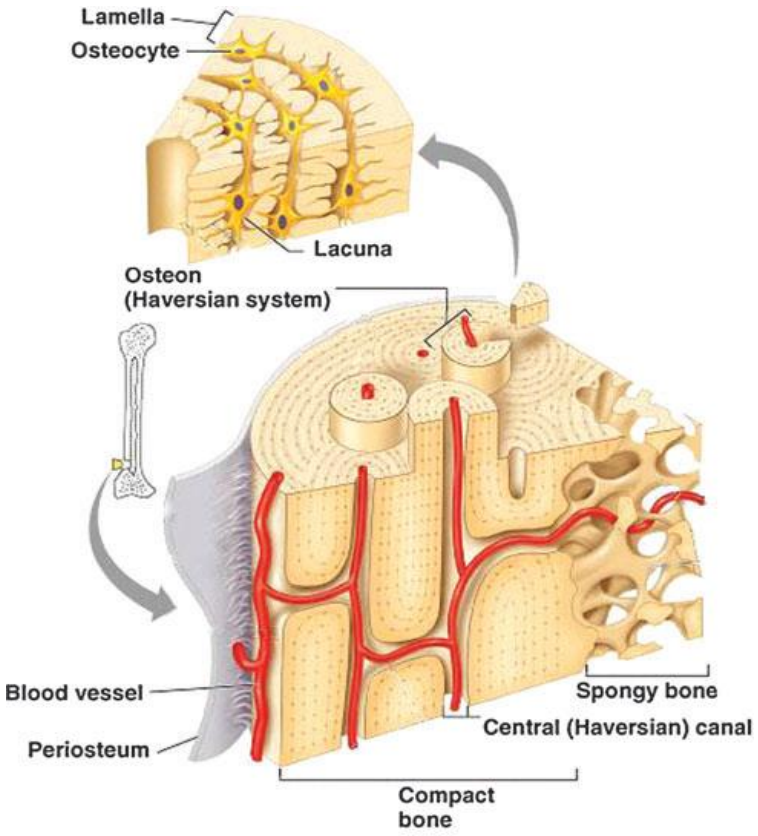

Figure 1: Schematic illustration of bone structure.
The human bone is fully vascularized, as blood vessels are spread through Harversian canals and Volkmann's canals that exist throughout the entire bone tissue [33-35]. These blood vessels play fundamental roles in bone tissue development by supplying oxygen, nutrients, hormones and osteoprogenitor cells that are necessary for supporting bone development, remodeling and fracture healing [24]. Figure taken from [27].

1.1.1 Bone regeneration

The human bone is a fully vascularized tissue with highly sophisticated self-healing properties. Blood vessels are spread throughout the Harversian canals and Volkmann's canals in the bone tissue [33-35]. These blood vessels play an important role in bone development, remodeling and fracture healing [24]. When bone tissue is damaged the process of angiogenesis and osteogenesis is started. These occur in a coupled manner, where the blood vessels play an important role in supporting the growth and activity of osteogenic cells [28]. Thus, the lack of adequate vascularization of bone scaffolds should be considered as one of the key reasons for the insufficient healing of bone defects and anomalies [26, 36].

The link between bone regeneration and vascularization will be further explained in the next sections.

1.1.1.1 Blood vascular system in bone

Depending on their composition and anatomical shape and structure, the long bone can be divided into three different parts called diaphysis, epiphysis and metaphysis. Diaphysis is a tube-like mast that extends along the ends of the bone and are mainly composed of cortical bone. Epiphysis are the wider edges and metaphysis is cone shaped structure between the epiphysis and the diaphysis [37]. Epiphysis and metaphysis are made mainly of trabecular bone and are enclosed by cortical bone [38, 39]. The exterior of the bone is enclosed by periosteum, whereas the inner layer is composed of endosteum. The periosteum, the connective tissue that surrounds the outside area of bone has a high number of nerves, blood vessels, osteoblasts and osteoclasts. Endosteum covers the inner surface of bone and vascular canals. This membranous structure contains protective bone lining cells that conceals the bone surface. It also comprises of connective tissue fibers and blood vessels that the bone requires for nutrients supply [37]. Diaphyseal, periosteal, metaphyseal and epiphyseal are the four different types of vascular networks of adult long bone. Arteries from the surrounding tissues enter the bone through various foramina/opening. These blood vessels enter through Volkmann's and Haversian canals and spread into cortical bone [40]. Diaphyseal artery is the main vessel that delivers over 50% of total blood that reaches the long bones [38, 41]. Diaphyseal artery enters the diaphysis through nutrient foramina and branches throughout the medullary cavity. The branches then extend and reach the epiphysis and finally split into minor ramifications. Metaphyseal arteries come into long bones along metaphysis. Epiphyseal arteries comprise the periarticular vascular arcades [39, 42]. Venous blood enters via the venous central sinus and departures the bone with the help of veins of the cortical bone collar [42]. This vascular system delivers oxygen, nutrients and osteoprogenitor cells to important terminal regions of the bone and maintains its functionality [43].

In the following sections the role of vascularization in bone development, during both fetal development and adult bone will be described, with special focus on the role of VEGF in these processes.

Vascularization is a key process that regulates osteogenesis in embryonic bone formation and adult bone fracture repair mechanisms. The skeletal development during embryonic development can be classified into two different mechanisms called intramembranous ossification and endochondral ossification. The important process of intramembranous ossification takes place during fetal growth of flat bones such as cranium flat bones, facial bones, mandible and clavicle bones [44]. Endochondral ossification is vital for the development and maturation of long bones [45]. Capillaries enter a mesenchymal zone during intramembranous ossification and induce the differentiation of MSCs to osteoblast cells. First the MSCs differentiate and form osteoprogenitor cells. Later these cells differentiate into osteoblast and express masker such as osteopontin, type I collagen and

osteocalcin, which are typical markers of bone matrix development [46].

The bone matrix deposition is repeated many times and leads to the creation of bone spicules, which develop and form trabeculae. This then forms woven bone, which is ultimately replaced by lamellar bone [47]. Long bones are formed by endochondral formation. During this process bone tissue is formed by the remodeling of hypertrophic cartilage. An existent cartilage template is used during endochondral ossification, during which the new skeletal tissue is formed by the invasion blood vessels by the existing cartilage tissue [48]. The long bone grows in both longitudinal direction and this growth is supported by the extension of the vascular system, which delivers the newly developing bone with important factors. During this developmental step, the newly developed capillaries are seen as column-like structures in the metaphysis and as a condensed sinusoidal web in the diaphysis [47]. During the fetal development of long bones, a mechanism known as mesenchymal pre-cartilage condensation takes place. This cartilage condensation process, leads to chondrogenesis [48]. This is the principal step in the expansion and development of skeletal tissues, which leads to the aggregation of MSCs and eventually their differentiation into cartilage [49]. Blood vessels then enter this cartilage substrate and chondrocytes are faced with hypertrophic environments. In this stage, chondrocytes also produce VEGF, which encourages further invasion of the vascular endothelium and recruits hematopoietic cells, osteoclasts and osteoblasts from the perichondrium [48]. These osteogenic cells collect together and develop a mineralized cartilage structure, which then replaces the hypertrophic cartilage with bone and the hypertrophic matrix is degraded [50-55]. Thus, understanding the developmental stages of vascularization during bone regeneration is indispensable when developing treatments to successfully induce bone regeneration in large defects [56, 57].

Vascularization also plays a crucial role during the process of adult bone repair. In adult bone repair, both angiogenesis and osteogenesis transpires in a coupled manner, which is similar to the development of embryonal bone tissues [58]. When fracture occurs to a mature bone, an inflammatory response is triggered. This activates growth factors and cytokines that attract osteoprogenitor cells to the site of defect. Initially a temporary clot is formed. This acts as a matrix from the ingrowth of vascular network. The clot is later replaced by fibro-cartilage and remodeled into new bone [59, 60], during which osteoclasts eliminate the leftover necrotic bone tissue and the normal blood circulation is reestablished via the process of angiogenesis. This repair mechanism has many similarities with the developmental process of the embryonic bone. The newly formed skeletal tissues primarily has physicochemical properties identical to the original bone tissue with formation of minimal scar tissue. The increase in formation of fibrous scar tissue can have deleterious effects on the mechanical properties of the newly restored bone tissue. Even though the repair mechanism may sometimes not be able to completely restore the original strength of the damaged bone, the complete absence of this process can have negative effects. Damage

to the musculoskeletal system leads to disruption of the vascular system as well. This can give rise to severe necrosis and hypoxia of the surrounding bone tissue [9, 61]. There are many important vascular growth factors. However, VEGF is the key player in angiogenesis as it can bind to receptors on endothelial cells and control cell fate. VEGF is also pivotal in inducing vascularization via endothelial cell signaling. They can also bind to osteoblast receptors and encourage bone reparation [57, 62]. Therefore, the cellular crosstalk between endothelial progenitor cells and MSCs by means of secreted proteins such as BMP-2 and VEGF is a critical mechanism that regulates the process of coupled osteogenesis and angiogenesis [63].

1.2 Current standards and bone tissue engineering approaches

Autografts are most commonly used in clinic today and are considered the gold standard. This is when the bone tissue is won from patient's body and transplanted into the required site [64]. These autografts are advantages, as they are patient derived and non-immunogenic. They also possess the native vascular and nervous network needed for support. The tissue in this case is able to provide proper osteogenic signals needed for the regenerative process [65, 66]. With their essential growth factors and cells, they support a rapid and efficient bone repair. But this method has its drawbacks, such as, donor site morbidity, possible infections, complications and pain [67]. Most importantly the limited amount of tissue that can be harvested is also an issue [68, 69]. The lack of ideal tissue engineered bone scaffolds results in poor regenerative capacity of the bone constructs and limits the clinical success [70].

It is known that the vascular system influence bone regeneration and repair [71]. Construction of bone implants that promote the formation of vascular networks can help repair large bone defects and help induce rapid repair of the damaged bone tissue. However, the improved vascularization of bone is still an issue that is needed to be tackled to able to engineer functional bone grafts for clinical application [70, 71]. Hence, more focus should be diverted towards finding ideal methods to combine both osteogenesis and vascularization techniques to fabricate the ideal tissue engineered bone construct. The following section will briefly explain the material properties of tissue engineered bone and focus on the current state of vascularized bone implants and their therapeutic opportunities.

1.2.1 Vascularized bone implants

The combination of osteogenesis and vascularization has already shown positive results in tissue engineering. Many investigators have demonstrated the use of microsurgical techniques to improve the vessel formation in tissue engineered bone constructs. Fan *et al.*

explained that the implantation of blood vessel into bone grafts, improved the osteogenesis of the tissue engineered bone *in vivo* [72]. Another promising example was presented by Feng *et al.* in their paper, where they studied how autologous blood vessels influenced vascularization and bone formation. They used a dog model and created inferior alveolar neurovascular-bundles or inferior alveolar nerves inside the mandibular canal. They then prepared a tissue engineered bone scaffold by injecting mesenchymal stem cells (MSCs) into β-tricalcium phosphate, which was finally fixed in place using a titanium mesh. This method showed improved regenerative capacity, with increased osteogenesis and vascularization [73].

A similar approach was shown by Chen and his colleagues. They were able to demonstrate that the implantation of a vascular bundle and sensory nerve bundle inside a tissue engineered bone was able to promote the osteogenesis of the bone construct and increase the expression levels of vasoactive intestinal peptide type 1 receptor and neurokinin 1 receptor [74]. These research results show that vascularization is an important player in successful development of tissue-engineered bone constructs.

There are three levels of graft integration with surrounding bone, which is illustrated in Figure 2(a). The first level resembles to osseointegration and is reliant on stability of the interphase and cellular activity. The next level is vascular integration and is essential for proper blood flow all over the scaffold. The final level involves slow replacement of the tissue engineered constructs by bone remodeling. This will allow the scaffold to fully integrate into the host tissue. Many bone tissue engineering strategies today focus on vascular repair and scaffold implantation as separate procedures [70, 72, 75]. But for better clinical results, the two concepts should be combined. For future tissue engineered bone constructs, new ideas that combine both the concepts should be given more attention, for example as described by Mercado-Pagán *et al*., as shown in Figure 2 (b). This group presented a new idea of combining a rigid bone scaffold with an integrated vascular graft within, which could enable continuous supply of nutrients to the scaffold. Additionally, they suggested to add cell-laden hydrogel that could supply the scaffold with cells [25].

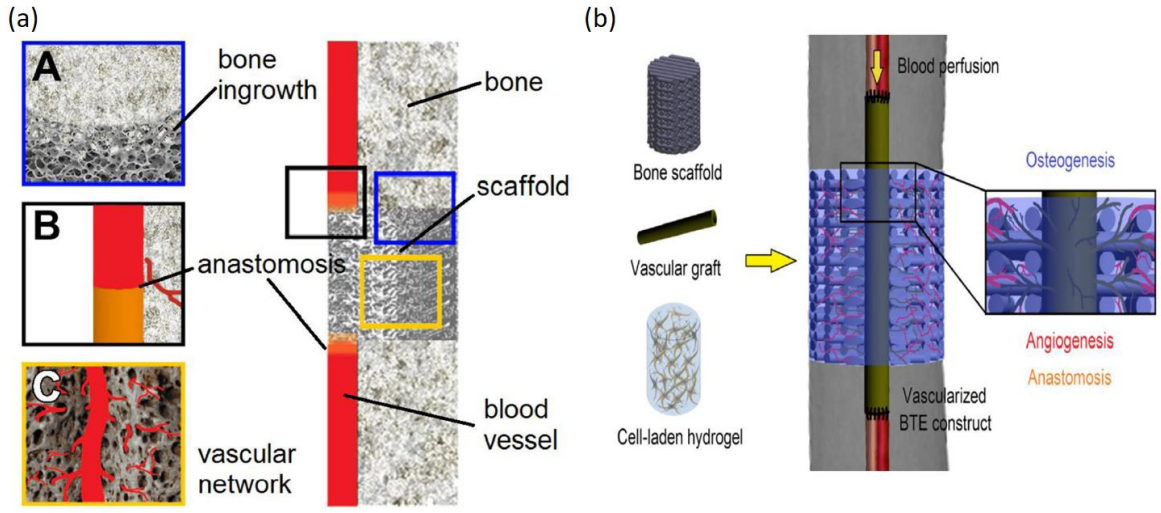

Figure 2: Schematic figure of vascularization of tissue engineered bone constructs.
(a) figure shows the integration of the tissue engineered graft into the native bone tissue. Levels: [A] osseointegration which is dependent on the stability of interphase and activity of the cell, [B] vascular anastomosis, which is the integration of the vascular network to allow blood flow all throughout the scaffold [C] vascular scaffold integration, where the scaffold is complete one with the surrounding. (b) A bone tissue engineering concept combined with vascularization approach [25]. Hydrogel with osteoblasts and a tissue engineered vascular graft are incorporated into a porous osteo-conductive solid frame. The surrounding hydrogel can deliver signals and cells needed for osteogenesis and vascularization. The vascular graft can provide blood supply and create microvascular beds in the hydrogel matrix. The solid construct acts as a scaffold for the cells to reside in and gives mechanical stability to the entire structure [25, 74, 76]. Figures taken from [25].

Bone angiogenesis and osteogenesis help and promote each other by crosstalk between cells [43, 77, 78]. Endothelial cells produce signals for osteoprogenitor cells (e.g., Notch signaling and hypoxia- inducible factor) [43, 77]. When human umbilical vein endothelial cells (HUVECs) and stem cells were co-cultured, HUVECs have shown to secrete BMP-2 and promote osteogenic differentiation [79]. Vascularization can also improve osteogenesis by supplying oxygen and nutrients to the surrounding bone tissue. It is known that in bone fractures, vessel growth and the invasion of osteoprogenitor cells are coupled [80]. Also, the amount of vessels and bone cells decrease during aging, reducing osteogenesis and increasing fracture incidence [81, 82]. Engineering an optimal bone tissue construct would enable enhanced oxygen and nutrient exchange required to make larger and more compatible tissue. Vascularization of the bone scaffold would fasten the rate of regeneration and facilitate their functional integration into the host tissue and thus lower the chance of hypoxia-induced cell death and degradation after transplantation [83]. In conclusion, the bone is a tissue with excellent regenerative ability [70] and this regenerative ability can be exploited when engineering bone structures by combining the concepts of innervation and vascularization of bone constructs [71, 72, 75].

1.2.2 Shear-thinning biomaterials

Hydrogels represent a highly promising biomaterial due to their properties such as high permeability, minimal invasion and biocompatibility. They can be easily synthesized using a range of different constituents and be molded to have physical characteristics that can be highly favorable for usage in regenerative medicine [84]. The development of an injectable self-healing and shear-thinning hydrogel that could promote rapid bone healing is a highly promising approach. The hydrogel has been shown to be biocompatible and can give rise to rapid osteogenesis [85]. A crucial requirement for a suitable hydrogel for bone tissue engineering is their easy synthesis, along with the possibility to fine tune their mechanical properties [11], [12].

1.2.2.1 Rheological characterization of shear-thinning gels

This section gives a short overview of the principal of rheology and how it can be used for the characterization of shear-thinning biomaterials (STB).

Shear thinning materials are a polymeric material that exhibit non-Newtonian behavior, wherein the viscosity of non-Newtonian fluids is reliant on the shear rate which is applied. When a specific shear rate is applied, the viscosity of the STB decreases with increasing shear rate. Thus, the solid biomaterial begins to flow. Additional exceptional characteristic of such materials is the reversibility of the shear-thinning effect. STBs will return to their solid state once the shear force is removed or reversed. Rheology is the quantitative evaluation of the way in which substances deform and flow under controlled testing parameters. Elastic or storage modulus (G') is an important term used to describe the elasticity of a substance and its ability to store energy when deformed. It is described using the formula: G' = (stress*/strain)cos Ɵ. G' is usually expressed in Pascals (Pa) [86, 87].

A Rheometer machine can be used to measure the behaviors of the desired shear-thinning materials. For example, a dynamic strain sweep experiment can be done to evaluate the effect of shear stress on shear-thinning behavior and relaxation behavior. The rheological properties of shear-thinning material are not affected by applied stain up to a critical stain level. After this level is reached, the material will change its behavior from linear to non-linear and the storage modulus will fall [87].

Rheology property is a highly significant material characteristic to evaluate the injectability of hydrogels. Rheology can be used to observe viscoelastic behavior in different formulations of shear-thinning hydrogels. Most studies use oscillatory rheological measurements to determine how sample conditions, molecule chemistry and environmental factors effect the gel kinetics and rigidity. Tests such as the oscillatory shear rheology can help describe the ability of the hydrogels to rapidly recover into solids once it has been injected and how

encapsulated cargos are affected by flow, which is important to consider for biomedical applications [86-89].

1.2.2.2 Silicate Clays as Bioactive Nanomaterials for bone regeneration

This section describes the concept of shear-thinning hydrogels that are composed of silicate nanoparticles and gelatin and how the special nanoparticles have the capability to enhance osteogenesis and thus may perhaps be a promising candidate for bone tissue engineering strategies.

Figure 3 (a) illustrates the shape and size of silicate nanoparticles. Silicate particles display a 2D platelet like structure that are around 1 nm in thickness and 25 to 30 nm in diameter. These particles have a have a distinct layered structure which gives it a permanent negative surface charge. This characteristic makes them highly useful for diverse biomedical applications [90]. The complementary affinity between the biopolymer, gelatin and the surface of the silicate nanoplatelets could be exploited to manufacture high water content and tunable hydrogels. This concept is illustrated in Figure 3 (b). The silicate based gels are self-healing, meaning when pressure is applied they can flow. When the pressure is released, the gel becomes solid. This is shown in Figure 3 (c), were the gel is injected though a needle, but once injected they seem to be solid and maintain their structural integrity. The self-healing behavior is shown with the help of rheological measurement in Figure 3 (d). The hydrogel was able to deform and form when subjected to alternating high and low strain conditions respectively [84].

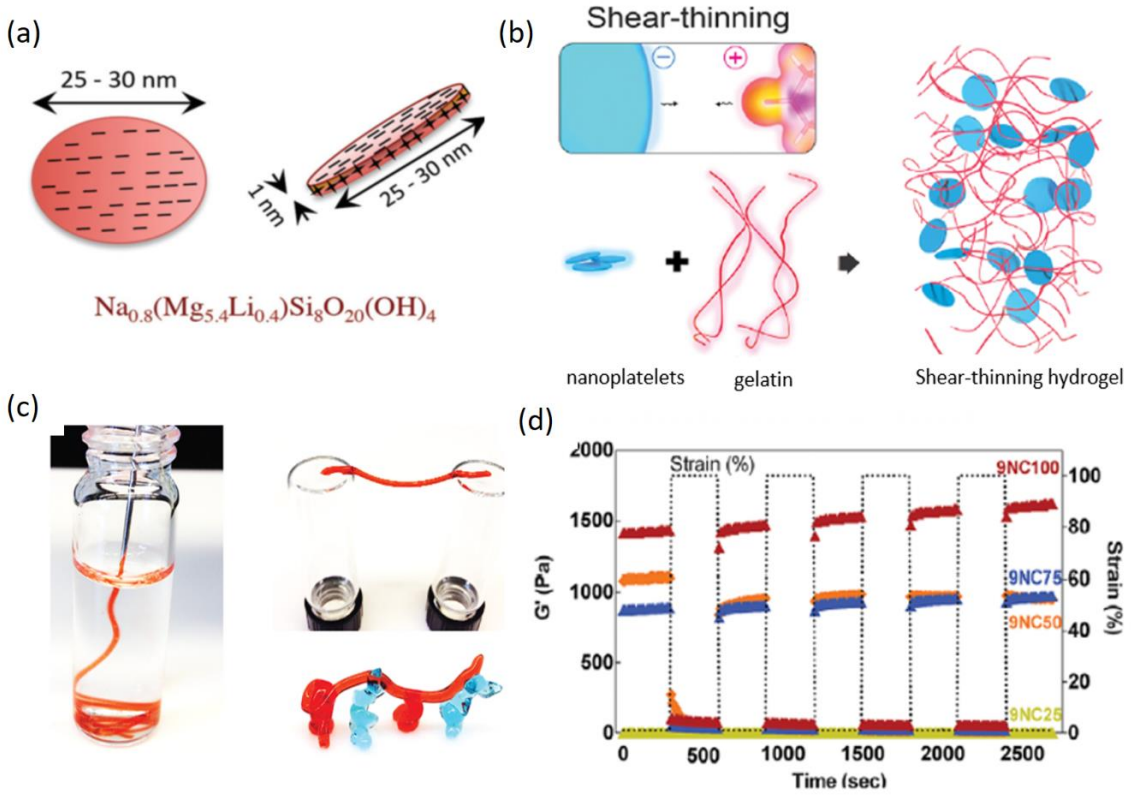

Figure 3: Shear-thinning hydrogel composed of silicate nanoparticles and gelatin.
(a) Schematic image of silicate nanoparticles [16]. The silicate nanoplatelets have a disc like structure. They are 25 to 30 nm in diameter and ~1 nm in width. Figure taken from [84] (b) silicate nanoparticles exhibit anisotropic charge distribution on their surface: negative on the top and bottom and positive along the edge. Due to this heterogeneous distribution of the surface charges, these nanoplatelets can form self-assembled gels in aqueous media (gelatin solution). Figure taken from [90]. (c) & (d) Self-healing behavior of gel is shown. When injection force is applied the gel can flow, whereas when the force is released the gel can form a solid mass. The self-healing behavior is shown by rheology measurement, using a Rheometer. Recovery of the nanocomposite gel was seen when the hydrogel was subjected to alternating high and low strain conditions in an alternating manner (100% strain and 1% strain). Figures taken from [84].

It has been established that silicate can improve the osteogenic differentiation of stem cells. This is illustrated in Figure 4. Increasing silicate nanoparticles concentration improves hierarchical microstructure of the produced scaffolds. This in turn enhances cell adhesion and spreading [90, 91] (see Figure 4 (a)). This is said to be contributed integrin binding of the cells, which is said to be mediated by magnesium ions. Gaharwar and his colleges where able to show that silicate can adhere to the surface and also be internalized by mesenchymal stem cells and this helped promote osteogenesis of the cells (see Figure 4 (b)). They also showed that silicate is a bioactive material that can increase matrix mineralization of cultured stem cells as seen in Figure 4 (c). The added complexity that the silicate particles add to the surface of the scaffold better mimics the microscale features of the native-tissue. As a result,

the mechanical stability is increased and permits sequestration of bioactive molecules for longer periods of application [90].

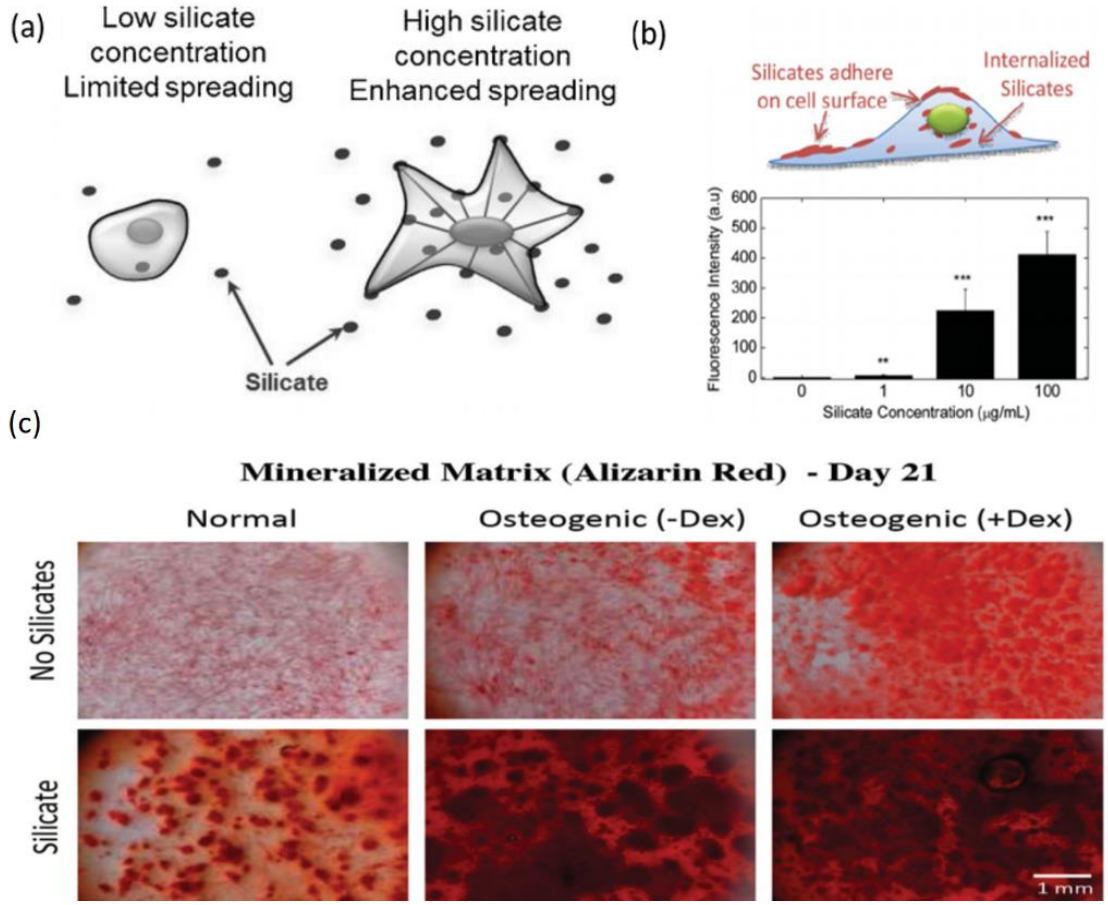

Figure 4: Nano-sized bioactive silicate particles induce osteogenic differentiation of stem cells.
(a) Higher concentrations of silicate have shown to improve cell spreading and adhesion. Silicate enables cell spreading probably by providing additional cell adhesion sites. Figure taken and modified from [92] (b) silicate particles can induce osteogenesis in mesenchymal stem cells, via cell contact and internalization. Figure adapted from [90] (c) The osteogenic effect of silicate on matrix mineralization is shown after staining with Alizarin Red. The stem cells where cultures in control media, osteogenic media or osteogenic media with addition of dextranamethasone, which is known to enhance osteogenesis. The images show that the increase in the amount of silicate nanoplatelets can significantly improve the mineralized matrix formation. Figure taken from [90].

1.3 Aim of the Thesis

The aim of this study will be to develop an injectable shear-thinning nanocomposite hydrogel composed of synthetically produced silicate nanoparticles and gelatin that can be employed for a range of biomedical and industrial applications. The scaffold will have a bone and vessel part with different silicate concentrations. The total solid concentration will be controlled to regulate the stiffness of STB. Additional, VEGF loaded polycaprolactone (PCL) particles will be added to the vessel part of the scaffold to help create a vasculogenic STBs. The schematic illustration of the study is seen in Figure 5. The bone part will contain mouse

osteoblast cells and the vessel part will have mouse endothelial cells. The cells will be cultured in the gel to evaluate their proliferation and viability.

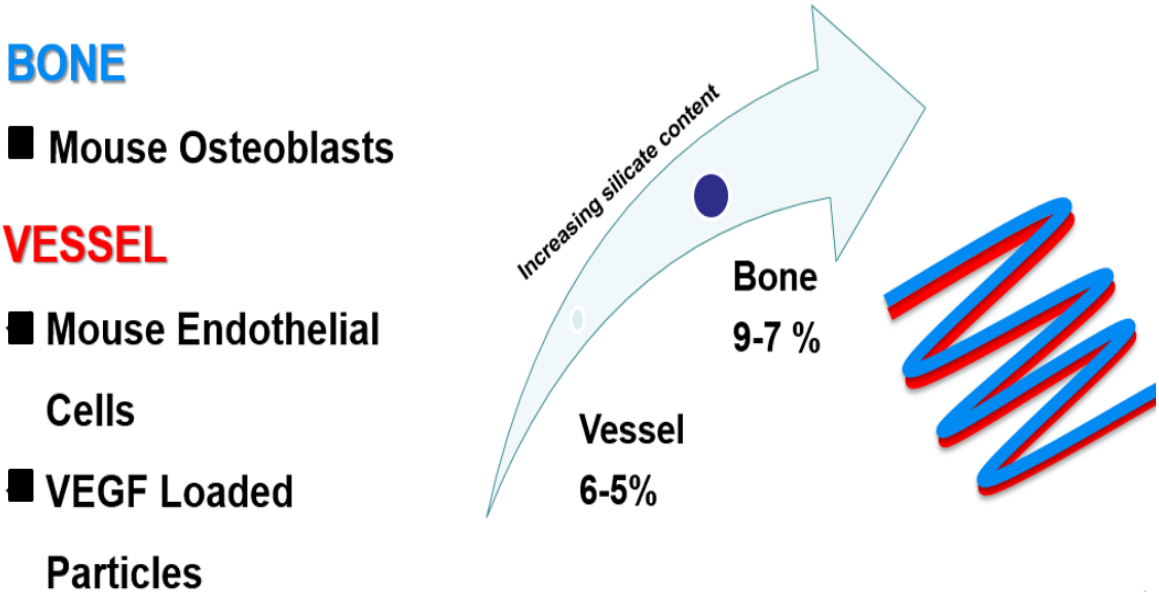

Figure 5: Experimental design to prepare a shear-thinning biomaterial for bone repair.
Bone and vessel parts will be prepared with incorporated cells, osteoblasts and endothelial cells respectively. Different concentrations of gel will be tested, with higher silicate concentration for the bone part and lower concentration for the vessel part.

It will be attempted to recreate the ideal microenvironment for the growth of both cell types. This will be done by regulating the composition of the STBs. The proposed STB will also be evaluated on its printability and shear-thinning properties. The STB should also be biocompatible to allow cells to proliferate and differentiate to form new bone tissue when applied *in vivo*.

Conclusively, this thesis focuses on the development of a silicate based shear-thinning biomaterial that can be used as a scaffold for bone regeneration. The main aims of this study are:

1) Preparation and *in vitro* characterization of VEGF loaded PCL particles
2) Engineering and characterization of shear thinning hydrogels
3) Gradient formation and 3D bioprinting of scaffolds
4) *In vitro* evaluation of these hydrogels for their biocompatibility and osteogenic potential

2 Materials and Methods

2.1 Materials and reagents

A detailed list of all used reagents and materials used can be found in the appendix.

2.2 Preparation of STB and PCL particles

2.2.1 Shear-thinning gel formulation

The STB gel was prepared according to the protocol described by the group of Gaharwar [9].

Stock solution of 9% (w/w) nanoplatelets and 18% (w/w) gelatin were prepared in distilled water. Firstly, 450 mg of laponite was measured on a scale (lab analytical balance digital precision scale, U.S. solid®). This powder was added to cold water (4 °C) to slow down the gelation rate of the nanoparticles. The mixture was then vortexed for 10 seconds using a vortexer (neoLab-Vortex Genie 2, 7-0092) at a maximum speed of 2700 revolutions per minute (rpm). The mixture was then centrifuged (Eppendorf 5810R Refrigerated Centrifuge) at 800 rpm for 15 min until clear gel was formed. For making the gelatin solution, 1.8 g of gelatin was dissolved in 10 ml distilled water and the mixture was mixed by vortexing. The solution was then placed in the oven (Gravity Convection Laboratory Ovens by Shel Lab) 80 °C for 10 min. Different STB formulations were prepared by weighing and mixing various concentrations of gelatin (18%, w/w), the nanoclay (9%, w/w) and water. The different concentrations that were prepared is listed in Table 1. After combining gelatin, water and silicate, the mixture was vortexed for 15 min to achieve a homogenous gel.

In the formulation code, NC stands for Nano-Composite and a total solid content of gel written in front of NC and the ratio of silicate present in this solid content written after NC. For example, 3NC50 has a solid content of 3%, 50% of which is silicate.

Table 1: Concentrations of gelatin, silicate and water used to make the different STB formulations.
The table shows different formulations of STBs that were tested. The volume of gelatin, silicate and water used to prepare each formulation is given. The NC of formulation code stands for Nano-Composite. Formulation code 3NC25 means, 3 is the total solid content and 25% of this solid content is silicate.

formulation code	gelatin (g)	nanosilicate (g)	water (ml)
3NC25	1.9	1.3	12.1
3NC50	1.3	2.5	11.5
3NC75	0.6	3.8	10.6
3,75NC25	1.9	1.3	9.05
3,75NC50	1.3	2.5	8.45
3,75NC75	0.6	3.8	7.6
4,5NC25	1.9	1.3	6.9

4,5NC50	1.3	2.5	6.3
4,5NC75	0.6	3.8	5.6
5NC25	1.9	1.3	5.98
5NC50	1.3	2.5	5.38
5NC75	1.8	11.4	13.8
6NC25	1.9	1.3	4.45
6NC50	1.3	2.5	3.85
6NC75	1.8	11.4	9.3
7NC25	1.9	1.3	2.92
7NC50	1.3	2.5	2.32
7NC75	1.8	11.4	4.8
8NC50	1.3	2.5	1.9
8NC75	0.6	3.8	1.2
9NC25	1.9	1.3	1.9
9NC50	1.3	2.5	1.3
9NC75	0.6	3.8	0.6
8NC50	1.3	2.5	1.33
8NC75	0.6	3.8	0.64
9NC25	1.9	1.3	1.39
9NC50	1.3	2.5	0.79
9NC75	0.6	3.8	0.1

2.2.2 Fabrication of PCL particles

Many different sizes of PCL nanoparticles were compounded by the double emulsion (W1/O/W2) solvent evaporation technique as described by Bilati *et al.* [93]. See Table 2 for detailed concentrations and setups used for each formulation. Firstly, 250 mg of PCL was dissolved in 5 ml Dichloromethane by shaking. Then, a 10 ml Polyvinyl Alcohol (PVA) solution containing 10 µg of Fluorescein isothiocyanate–dextrantran (FITC-Dextran) and 25 µg of Bovine serum albumin (BSA) as a stabilizer was emulsified in a mixture of PCL and methylene chloride using a probe-type ultrasonic homogenizer (Qsonica Sonicator, #Q500, Newton, CT, USA) at 50 W for 1 min. This primary emulsion was re-emulsified in 150 ml of 0.1% (w/v) PVA solution using ultrasonic homogenizer for at 50 W 3 min and then stirred for 2 hours using a magnetic stirrer (AccuPlate™ Digital Stirrer) to evaporate the organic solvent completely. The obtained particles were collected by centrifugation (Eppendorf Centrifuge 5427 Refrigerated). After centrifugation, the samples were washed three times with distilled water and finally lyophilized for 2 days (FreeZone 1 Liter Benchtop Freeze Dry System).

Table 2: Experimental Plan for preparing PCL particles

The parameters used for making 3 different PCL particles are listed. The different ultrasonication amplitudes and times are applied to make particles of different sizes.

formulation code	PCL amount (mg)	dichloromethane(ml)	BSA (mg)	PVA (ml) (Internal)	PVA (ml)
F	250	5	25	10	30

Formulation Code	Ultrasonification Amplitude (%)	Ultrasonification Time (min)	Stirring Speed (rpm)	Evaporation Time (hour)	Centrifugation (rpm)	Expected Particle size (nm)
F1	50	5	750	2	7500	~200
F2	40	3				~500
F3	30	1				~700

For making the VEGF loaded PCL particles, the FITC-Dextran and the BSA was replaced by 10 µg of VEGF.

2.2.2.1 Characterization of PCL nanoparticles

2.2.2.1.1 Morphological characterization of PCL particles by field emission scanning electron microscope (SEM)

The freeze-dried PCL particles were tested for their morphological properties by using SEM. First, the coverslips were mounted onto aluminum stubs and a small amount of the freeze-dried PCL samples were placed on it. After this, the samples were gold-coated with 10 nm thickness and acceleration voltages at the range of 5kV to 10Kv were applied. Then, the structure and morphology of the PCL particles were assessed by SEM (Ultra 55, Zeiss) and images were taken.

2.2.2.1.2 Release Profile from PCL nanoparticles

The release behavior of the three sizes of PCL particles where measured. Three different sizes ranging from large, medium to small were tested. The sizes analyzed were F1, F2 and F3. FITC-dextran (20 kDa molecular weight) was encapsulated in the PCL particles using the previously described double emulsion method. The release studies were carried out. Firstly, 50 mg nanoparticles was transferred to a 1.5 ml Eppendorf tube. Then 200 µl of distilled water was added to the tube. After this step the samples were kept in the incubator at 37 ºC. For measurement, the tubes were centrifuged and supernatant was collected for analysis every day at the same timepoint. For this purpose, 100 µl of supernatant was removed and added to a well of a 96 well plate and the samples were read using a microplate reader (Synergy 2, Biotek). The fluorescent intensity was measured at 495 nm Excitation and 519 nm Emission wavelength. The same samples were added back to the release tube immediately after each sampling to maintain constant conditions. The release profiles of the

particles were measured for 7 days. Finally, the cumulative release was measured each day and the data was collected. The experiment was conducted in triplicates.

2.2.2.1.3 Visualization of particles under florescent microscope

To visualize the particles under a fluorescent microscope, the F1 particles where encapsulated with FITC-dextran. The previously described procedure was used for encapsulation. The particles were however not freeze-dried, but only centrifuged. A small volume of particles was taken and spread evenly on a glass slide. Then the particles were visualized under the microscope and the green fluorescent channel was used for imaging.

2.3 Characterization of Shear-thinning gel formulation

2.3.1 3D Printing of STB

For the 3D printing the STB the scaffolds, the continuous multi-material extrusion bioprinter, as described by the group of Liu was used [94] . Two different concentrations of STB, 7NC50 and 6NC50 were loaded into reservoirs (see *Figure 6*). After, this the used according to the description by Liu and his group. The custom made multi-material bioprinting device was composed of multiple reservoirs that were loaded with different STB types. The printer was started and a pressure of 40 kPa was set on the pressure valve. The STB was ejected from the print head of the reservoir. Images of the printed scaffold was using a camera (canon compact digital camera, IXUS).

First, it was attempted to print the STB, during which different pressure setups were tested on the printer. Once the parameter for printing was finalized, colored dye was added to the STB and colored patterned structures were printed. The STB was also mixed with fluorescent beads to visualize the scaffold interface between the bone and vessel part. These fluorescent scaffolds were visualized under the UV light and the fluorescence microscope.

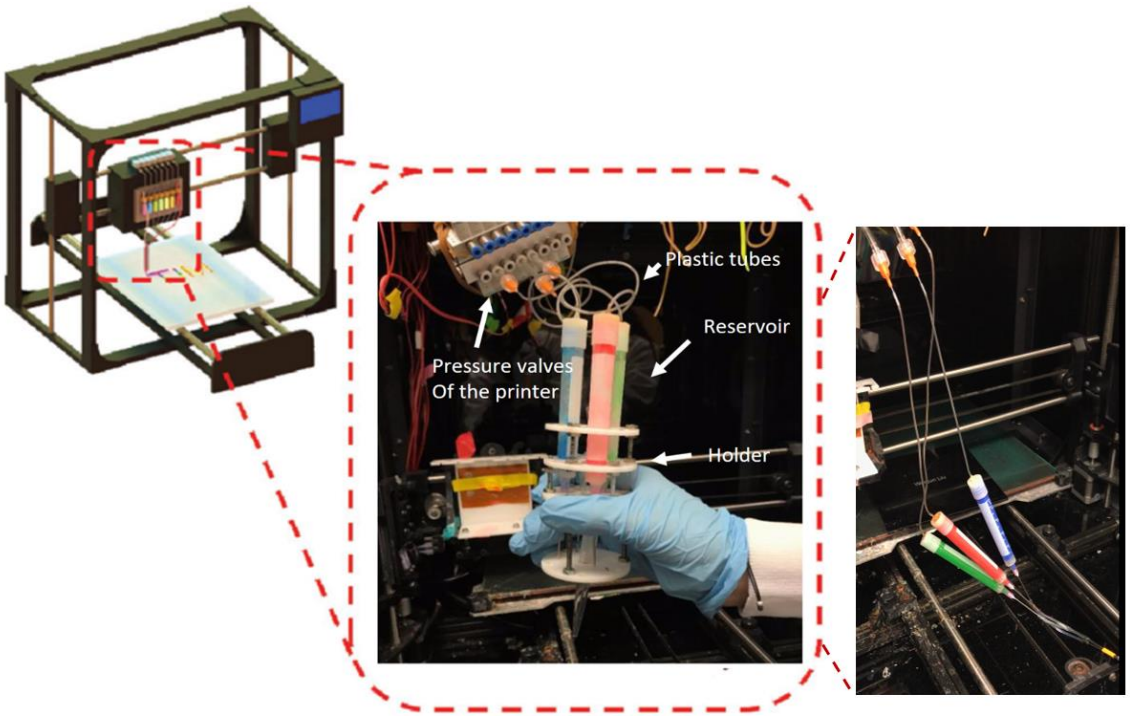

Figure 6: Printing of STB with the multi-channel bioprinter (schematic image of bioprinter modified from [94])

Reservoirs as seen in the image were placed on the holder. The top of the reservoirs were connected to the pressure valves of the bioprinter via plastic tubes. The closing and opening of the valves could be regulated on the control panel of the printer. Different concentrations of gels were loaded into reservoirs. The reservoirs had 18-gauge needles attached to their ends, which were joined together using a 1 ml pipet tip, to make the gels combine when coming out. When a pressure valve was opened, the corresponding STB was printed.

Visualization of STB interphase with fluorescent beads

To visualize the STB interphases, three different formulations were made. First, STBs of concentrations 7NC50, 6NC50 and 5NC50 were made as previously described and fluorescent dyes were added to them. 7NC50 (blue), 6NC50 (red) and 5NC50 (green) gels where printed with the multi-channel bioprinter and placed on a glass slide. The scaffold was visualized under the UV lap and pictures were taken. The interphase of the gels, was also visualized under a fluorescence microscope.

2.3.2 Injectability of shear-thinning gels with different sizes of PCL nanoparticles

The injectability of the STB was analyzed using an Intron machine (Instron Model 5542). First, 3 different sizes of PCL particles were mixed with the STB at the concentration of 1.25 mg/ml gel. After this the prepared STB samples were loaded into 3 ml plastic syringes (ID, 8.66 mm; BD Biosciences) and injected through needles (18-gauge, BD Biosciences). The desired flow rates were achieved by controlling the injection rate. This was achieved by

changing the cross speed of the compression platen. The data was recorded and plotted. The experimental setup schematic representation can be seen in Figure 7 and was performed as depicted by Reginald *et al.,* 2016.

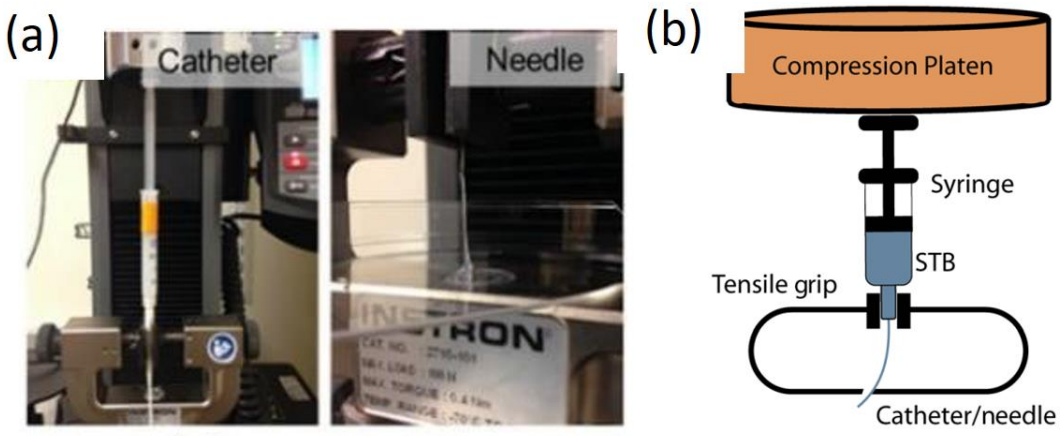

Figure 7: Setup for measuring the injection force using an Instron mechanical tester.
(a)The injectability of the STB can be analyzed using an Instron mechanical tester. (b) The gel was added to the syringe, which was secured on the Intron with a grip. The syringe was then pushed down using the upper compression platen. Figures adapted from [95].

2.3.3 Rheological Analysis of STB

Rheology tests were performed to evaluate the shear-thinning properties of the STBs. The measurements would give insight into how the varying silicate content and the presence of PCL particles effected the shear-thinning behavior of the gels.

Rheological properties were characterized using an Anton Paar MCR-301 rheometer equipped with a 20-mm diameter parallel plate geometry and a gap of 500 µm. All tests were conducted at 37 ºC. A small volume of the sample was loaded onto the lower plate of the rheometer (~100 µl). To avoid evaporation of water from the sample, a thin layer of mineral oil was put around the border of the plate. Firstly, strain sweeps test was performed from 0.1% to 1000% strain at 1 hertz. This test would give information about of the material's linearity and till what stain levels it can stay intact. Recovery of the STB was determined by performing 100% stain for 5 min, followed by 1% strain at a frequency of 1 Hz. This was repeated 4 times to acquire a continues rheology graph showing the shear-thinning and recovery behavior of the gel. When stress is applied the shear-thinning characteristic should help the gel deform and under zero stress the self-healing property of the gel should help it heal.

2.4 Co-culture of osteoblast and endothelial cells

2.4.1 Cell culture conditions

Two cell types were used for the experiments. Mouse osteoblasts (MC3T3-E1, Sigma) and BALB/c Mouse Primary Mammary Microvascular Endothelial Cells (BALB-5020, Cell Biologics). Cells of passage 6-8 were used for the experiments.

The cells were received frozen and expanded before starting the experiments. The cryovials containing the cells were removed from the -185 °C liquid nitrogen. They were thawed by placing the cryotubes in water at 37°C, enabling a fast defrosting of the cells, to prevent damage. The cell suspension was immediately transferred to growth medium [DMEM, 2 % FCS, 1% Penicillin/Streptomycin] and centrifuged for 5 minutes at 1200rpm. The supernatant was removed and the cell pellet was suspended in fresh growth medium and seeded on culture plates for monolayer cell culture and media was added.

Osteoblasts were cultured in Dulbecco's modified Eagle medium (DMEM, Gibco) supplemented with 10% fetal bovine serum and 1% penicillin– streptomycin. Endothelial cells were cultured in Endothelial Cell Medium with Supplement Kit (Cat No M1168, Cell Biologics). Osteoblasts and endothelial cells were cultured in 5% CO_2 humidified incubators at 37 °C. The media was changed 3 times per week and the cells were passaged once per week when they reached 80% confluency.
For passaging or cell counting, the medium was removed and the cells were washed with Dulbecco's phosphate-buffered saline (PBS). PBS was discarded and 1x trypsin-ethylene-diamine-tetra-acetic acid (EDTA) was added to cove the bottom of the plate. Then the dish was incubated for 5 minutes in a 5% CO_2 incubator at 37°C. Afterwards, medium was added (double the amount as trypsin used) and resuspended using a serological pipette.
Next, the cells were counted. 6 ml of the cell suspension were transferred into a 15 ml centrifugal tube. Centrifugation was performed at 1200 rpm for 5 minutes. Medium was carefully removed using a pipette. 8 ml media were added to resuspend the pellet. 10 µL of this solution were pipetted onto the Neubauer chamber and counting was performed under a light microscope.
Cells were either split 1:4 in a new culture dish with fresh complete medium or used for further experiments.

2.4.2 *In Vitro* 3D Cell Studies

For the *in vitro* studies, the experiment was repeated several times with the monoculture of osteoblasts to optimize the culture conditions and protocols, such as live/dead staining and PrestoBlue assay. For these studies, the cells were seeded at a concentration of 2 million cells/ml gel and basic growth media was used to culture the cell-laden scaffolds. The experimental design was the same as for the co-culture, which is explained below.

For the *in vitro* studies, the osteoblasts were seeded in 7NC50 gel and the endothelial cells were seeded in 6NC50 gels. A cell seeding ratio of 1:1 was used for all experiments. The following 6 groups were tested:

1. Co-culture of osteoblasts in 7NC50 (Passage 7-8) and primary mouse endothelial cells (passage 6) in 6NC50
2. Co-culture of osteoblasts in 7NC50 (Passage 7-8) and primary mouse endothelial cells (passage 6) in 6NC50 with PCL particles size F1 in gel (1.25 mg particles/ml of gel)
3. Mono-culture of osteoblasts in 7NC50 (Passage 7-8)
4. Mono-culture of osteoblasts in 7NC50 (Passage 7-8) with PCL particles size F1 in gel (1.25 mg particles /ml of gel)
5. Mono-culture of primary mouse endothelial cells (passage 6) in 6NC50
6. Mono-culture of primary mouse endothelial cells (passage 6) in 6NC50 with PCL particles of size F1 in gel (1.25 mg particles/ml of gel)

which composed of co-culture and mono-culture of the cells with/without PCL particles. The VEGF loaded particles were added at the concentration of 1.25 mg/ml of gel. The cell/gel construct was put into a syringe with an 18-gauge needle. The needle tips were combined using a plastic tube to achieve a continuous structure while injecting. The gel with encapsulated cells was injected into the wells of a 48 well plate (200 µl scaffold per well). The cell/gel constructs were covered with 500 µL culture medium. This experiment was performed twice, once with empty PCL particles (2 million cells used per ml gel) and additionally with VEGF loaded PCL particles (5 million cells used per ml gel).

For the empty PCL experiment, the scaffolds were culture in both osteoblast and endothelial cell media at a ratio of 1:1. To culture the cell-laden scaffolds with VEGF loaded particles, only osteoblast media was used.

2.4.2.1 Biocompatibility of PCL STG

2.4.2.1.1 Live/dead assay

Live/dead assay is a useful method to evaluate the viability of the cells in culture. Calcein-AM, can pass through the cell membranes of living cells. Where, it can be converted by intracellular esterases into fluorescein analogs with green fluorescence. Whereas, ethidium bromide (EB) only visualizes dead cells [96]. The Live/Dead assay was performed according to the manufacturer's instructions on day 1, 3 and 7. A cell density of 2 million per ml gel was used. Briefly, the cells were stained with Calcein AM (green) for live cells and ethidium homodimer-1 (red) for dead cells in PBS. The samples were incubated at 37 °C for 20 min and afterward washed with PBS for three times to complete the staining. The stained cells were imaged using an inverted fluorescence microscope (Zeiss Axio observer D1,

Thornwood, New York, NY, USA). The numbers of live and dead cells were calculated by analyzing the acquired six images from three different nanocomposite samples for each condition using NIH Image J Software. The cell viability was calculated as the percentage of the number of live cells to the total cells number.

2.4.2.1.2 PrestoBlue cell proliferation analysis

PrestoBlue cell viability reagent was used to evaluate cell metabolic activity. The assay was performed according to manufacturer's instructions on day 1, 3 and 7. A cell density of 5 million per ml gel was used for the experiment with VEGF particles. The samples were rinsed after removing the media. Then added 500 µl PrestoBlue solution, which was prepared at a concentration of 1:10 with media, was added to each well. After this the scaffolds were incubated at 37 °C for 2 h. 100 µl of the solution was transferred to wells of a 96-well plate. Then the absorbance was read at 530 nm for excitation and 590 nm for emission on using a plate reader (Synergy 2, HT-Reader, BioTek, Winooski). For each condition, the samples were tested in triplicates.

2.4.2.1.3 Cell tracker analysis

Osteoblast were labeled with green CMFDA cell tracker (C2925, Molecular Probes, Invitrogen, Canada) and endothelial cells were labeled with red CMTPX cell tracker (C34552, Molecular Probes) according to the manufacturer's protocol. To prepare 10 mM working concentration, 10 mM concentration of the Cell Tracker dye in DMSO was further diluted in DMEM. The cells were incubated in 1 mL of dye solution for 30 min at 37 °C in 5% CO_2. Then the cell suspension was centrifuged for 5 min at 1200 rpm and the pellet was washed two times with DMEM. A seeding density 2 million per ml gel was used with 1:1 ratio. The gels were plated in a 48 well plate (200 µl scaffold per well). The cell/gel constructs were overlaid with 500 µL culture medium. The cell/gel constructs were observed under a florescence microscope (Zeiss Axio observer D1, Thornwood, New York, NY, USA) on day 1, 3, 7 and 21.

2.4.2.2 Actin/DAPI staining to assess cell morphology

An Actin staining was performed to determine the structure of the cytoskeleton and DAPI was used to visualize the nucleus of the cells. Stainings were performed on day 1, 3 and 7. A cell density of 2 million per ml gel was used. Firstly, the media was removed and the scaffolds were washed with PBS. Later, PBS was removed and the scaffolds were incubated for 15 minutes in 4% Paraformaldehyde to fix the cells. Afterwards, the samples were washed 3 times with PBS (5 min) and permeabilized with Triton X 100 (PBS with 0.1% Triton X 100). After permeabilization the scaffolds were washed 3 times with PBS (5 min). Unspecific bindings were blocked by adding 1% BSA in PBS to the scaffolds for 2 hours (37°C, 5 % CO_2 and 100 % humidity).

The blocking solution was removed. For staining, Actin stock solution was diluted 1:40 in PBS with 1% BSA for 20 minutes. Incubation was performed in the dark. Afterwards, scaffolds were counter stained with DAPI, 1:500 in PBS with 1% BSA for 5 minutes in the dark. The solution was removed and the scaffolds were washed with PBS twice. The samples were observed under a florescence microscope (Zeiss Axio observer D1, Thornwood, New York, NY, USA).

2.4.2.3 Gene Expression of co-culture of cells in scaffold

RNA isolation

For evaluation of the gene expression patterns, scaffolds were sampled on day 1 and day 7. RNA extraction was performed using the Trizol method. The scaffolds were chopped into small pieces and Trizol was added for 10 minutes at room temperature to maintain the RNA integrity while disrupting cells and solubilizing cell components. In the next step chloroform was added to the samples and mixed with a vortexer and the samples were incubated for 15 minutes at room temperature. Afterwards samples were centrifuged at 12000 rpm for 15 minutes at 4°C. Chloroform with following centrifugation separates the solution into an aqueous phase and anorganic phase. The upper aqueous phase which contains the RNA was transferred to a fresh Eppendorf tube. The RNA is recovered by precipitation with the same amount of isopropanol for 10 minutes at room temperature. The precipitated RNA was collected by centrifugation at 12000 rpm for 30 minutes at 4 °C. The pellet was washed with 70% ethanol and centrifuged at 12000 rpm for 8 minutes at 4 °C and the ethanol supernatant was removes. To ensure high quality of RNA this step was repeated. The RNA pellet was suspended in DEPEC water and incubated for 10 minutes at 40°C. The RNA concentration was measured using the NanoDrop photometer and the samples were stored at -80°C in the freezer until further analysis (which was not performed during this thesis).

2.5 Statistics

Statistical analysis was performed using GraphPad Prism 6. Data are presented as the mean ±/+ standard deviation. A sample number of $n \geq 3$ was used for all experiments. For comparison between groups the one-Way ANOVA Test was applied, if not otherwise stated. Differences between groups were considered statistically significant at $p < 0.05$. If data are not marked by an asterisk (*), differences were not statistically significant.

3 Results

3.1 Characterization of PCL nanoparticles

3.1.1 Morphological characterization of PCL particles by SEM

To optimize which PCL particles would be used for further studies, various experiments were performed to evaluate their properties. The three PCL particles F1, F2 and F3 were prepared as described and SEM analysis was done to visualize the morphological properties of the particles (see Figure 8 and Figure 9).

Figure 8 (a) shows PCL polymer droplets in their raw state before being used for fabrication of nanoparticles. First, only F2 particles were prepared to optimize the protocol. These particles displayed ideal spherical structure and seemed to have formed uniformly sized particles.

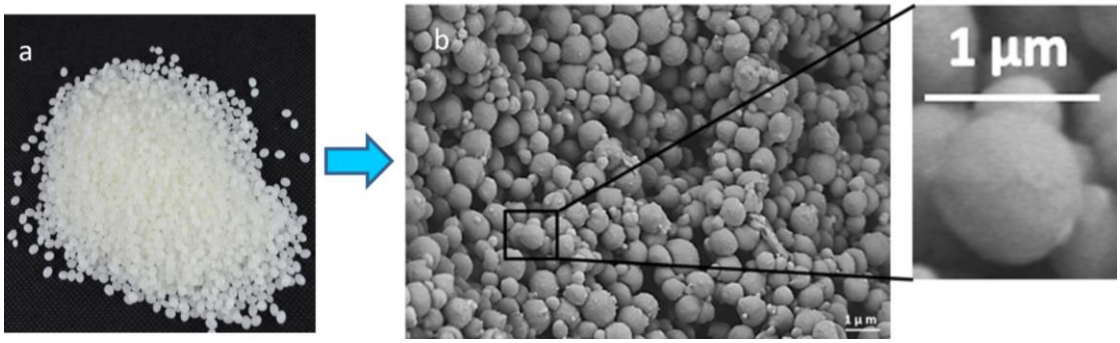

Figure 8: Fabrication of PLC nanoparticles by the double emulsion method using ultrasonication.
(a) Image shows PCL polymer in its raw state before being fabricated into nanoparticles. (b) SEM images of F2 particles were taken to visualize the structure and integrity of the particles. F2 particles were freeze-dried, sputter coated and analyzed by SEM to visualize the structure and integrity of the particles. 30 K X magnification: 30 000-fold magnification.

SEM images (see Figure 8 (b) and Figure 9) showed that all three particles where able to form capsules with intact spherical structure. The particles seem to have smooth surfaces with an almost perfect spherical shape. Very few particles were seen damaged, even though the samples had to undergo many different treatments to be analyzed with SEM. From the SEM images, it was concluded that all three particles were stable enough to be used for further experiments. Thus, additional tests had to be performed to choose the right particle size. The different amplitude settings and ultrasonication time clearly influenced the size of the prepared particles. Higher amplitude of 50% for 5 min lead to the formation of the smaller particles of ~ 200 nm (F1). The amplitude of 40% for 3 min, formed medium size particles of ~ 500 nm. The largest particles, F3 (~700 nm) were formed when using a low amplitude of 30% for 1 min.

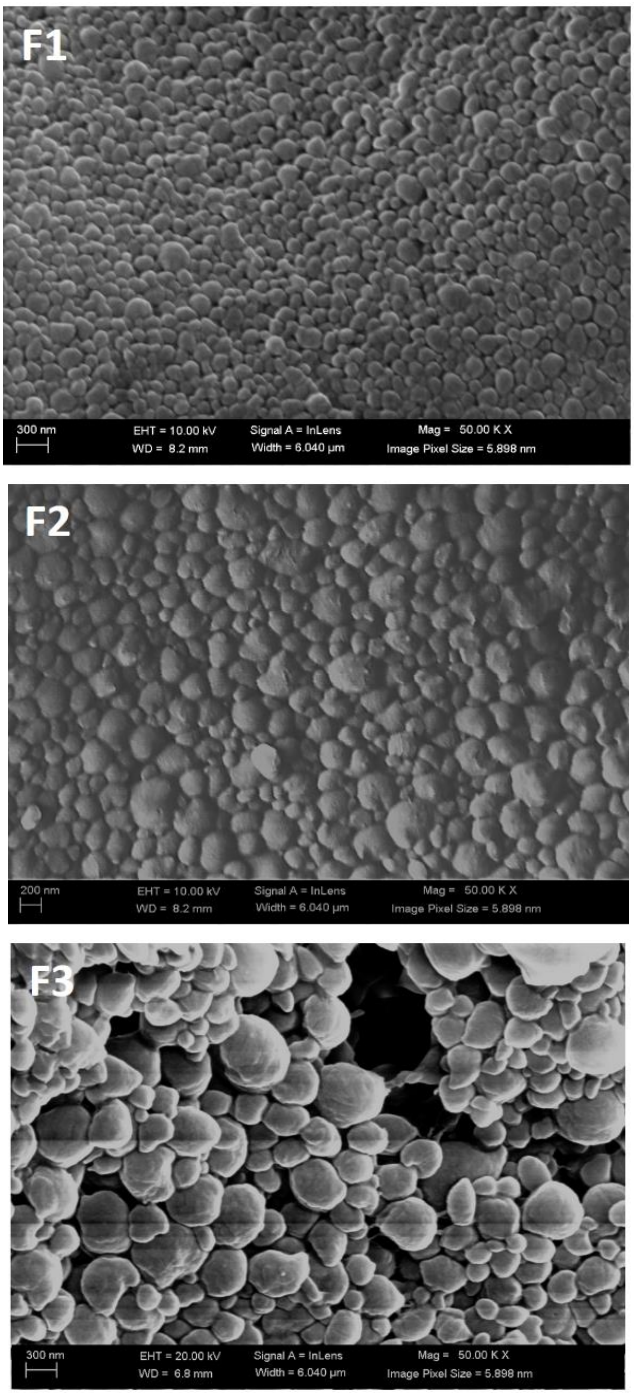

Figure 9: SEM images of F1, F2 and F3 PCL particles.

SEM analysis was performed to visualize the structure and integrity of the particles. The samples were freeze-dried, then sputter coated before analyzing them with SEM. All analyzed particles have different sizes. The F1 particles are ~200 nm in diameter, F2 particles are ~500 nm in diameter and F3 are the largest particles ~700 nm in diameter. The images were acquired with 50 000-fold magnification.

PCL particles were encapsulated within the STB to analyze how the particles interact with the surface of STB and if the particle morphology and stability was influenced by the contact

with the gel. Figure 10 shows F1 particles bound to the STB surface. The particles were added to the gel at a concentration of 1.25 mg/ml gel and freeze- dried before analysis. The PCL structure is still stable and no ruptures were seen on the particle surface. However, it was noted that the particles seemed to be stuck together at some spots. This could be due to inadequate mixing of the PCL and gel or the general aggregation of the particles due to their surface attraction. The SEM shows spherical particles with smooth surfaces.

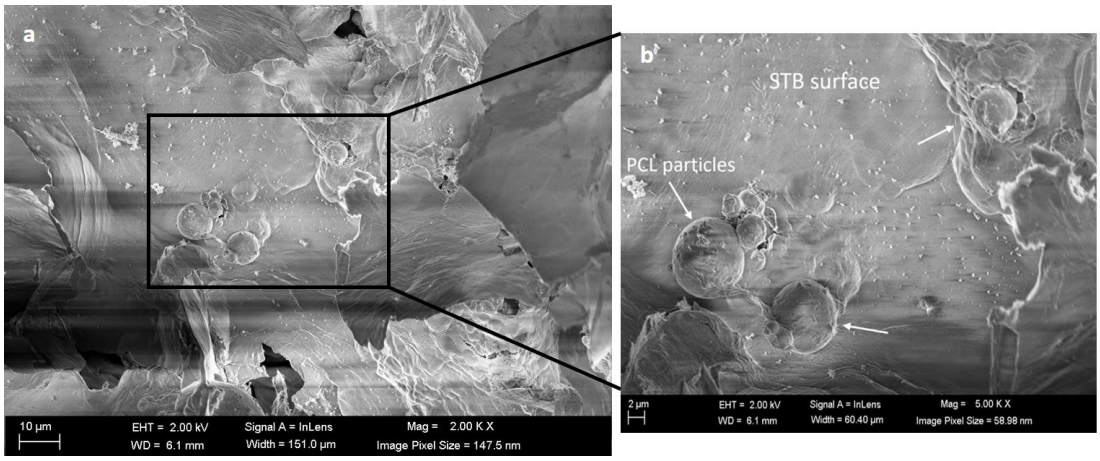

Figure 10: SEM image of F1 particles on STB surface.

(a) PCL particles are shown on the surface of the gel at 2000-fold magnification (b) magnified image of (a) acquired at 5000-fold magnification. The PCL particles were added to the STB at a concentration of 1.25 mg/ml and the gel was freeze dried for 2 days after which the images were acquired. The particles are incorporated into the gel surface and still maintain their spherical structure intact. The F1 particles of ~200 nm was used with 7NC50 gels.

3.1.2 3D Bioprinting of Shear-thinning nanocomposite

Printability of STBs were tested using the continuous multi-material extrusion bioprinter, as described by the group of Liu [94]. This printer allowed the formation of scaffolds with various gradient and layered structures. The STB to be printed and the speed at which it was printed could reregulated using the printers control panel. The printer allowed different valves to be opened or closed and the pressure to be regulated. The printer also has the possibility to be programmed to print specific patterns without any manual intervention. This aspect was not explored during this study. Figure 11 shows the possible patterned structures that can be derived using the multi-material printer. To optimize the printing parameters, many different gel compositions were tested. All gel formulation listed in Table 1 were fabricated and tested with the printer.

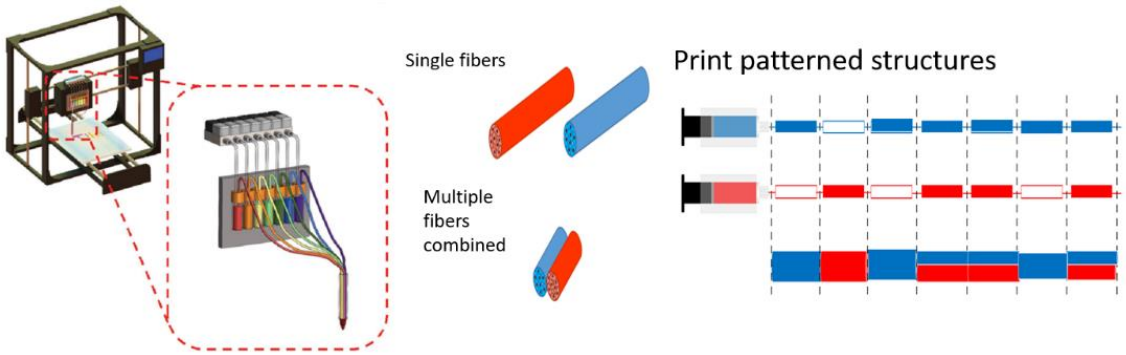

Figure 11: Continuous multi-material extrusion bioprinter.
Schematic figure showing the design of the seven-channel print-head connected to reservoirs that are individually actuated by programmable pneumatic valves and sample code for continuous bioprinting of a single microfiber consisting of one to seven types of silicate-based hydrogel ink. Bioprinting of patterned blood-vessel like structures, multi-layered blocks with continuous segments of different hydrogel inks possible due to the process of generating coded fibers. Figures modified from [94].

Different needle sizes were tested. It was seen it was difficult to print with smaller size needles, as they would often get clogged. Thus, the larger size needle with 18-gauge was chosen for the printing experiments. The different gels were filled in their respective reservoirs, which were connected to the pressure valves of the printer. When the valves were manually opened using the control panel on the printer, the desired gel would be injected out.

Figure 12 shows the gel, 5NC50 being printed as single layer. The gel recovered its structure after printing and did not mix with the surrounding water.

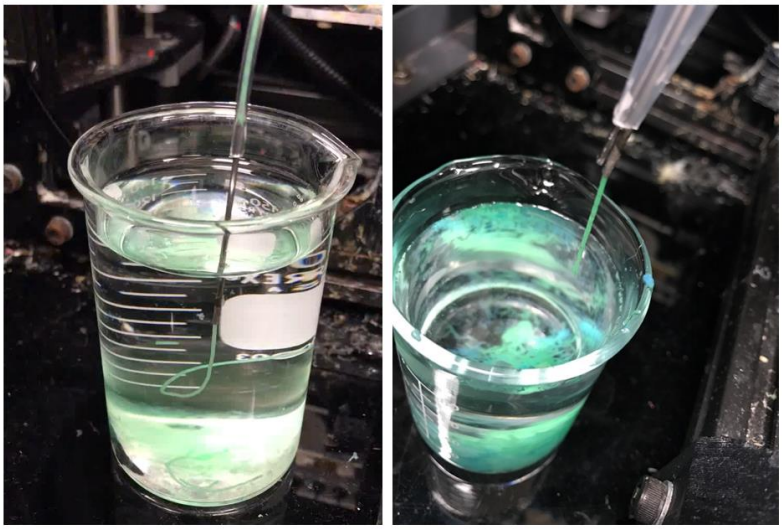

Figure 12: 3D printing of single layer structures.
3D printing of single layer structures of the shear-thinning gel using the multi-material extrusion bioprinter. 5NC50 (green) STBs were printed using the pressure ~35 kPa. The gel was printed at a steady speed and remained intact once printed.

All three valves could be simultaneously opened to make three gel layers with 7NC50, 6NC50 and 5NC50 (see *Figure 13*). The speed at which the gel was ejected out could be controlled by regulating the pressure applied. The tip of the needles were joined by pushing them into a 1ml pipette tip. This allowed the gels to come out together, forming a unified structure. However, the gel with 5% solid content was less viscous than the other two gels being printed. Hence, this STB would eject out faster than the other two. Thus, for further experiments only 7% and 6% gels were chosen.

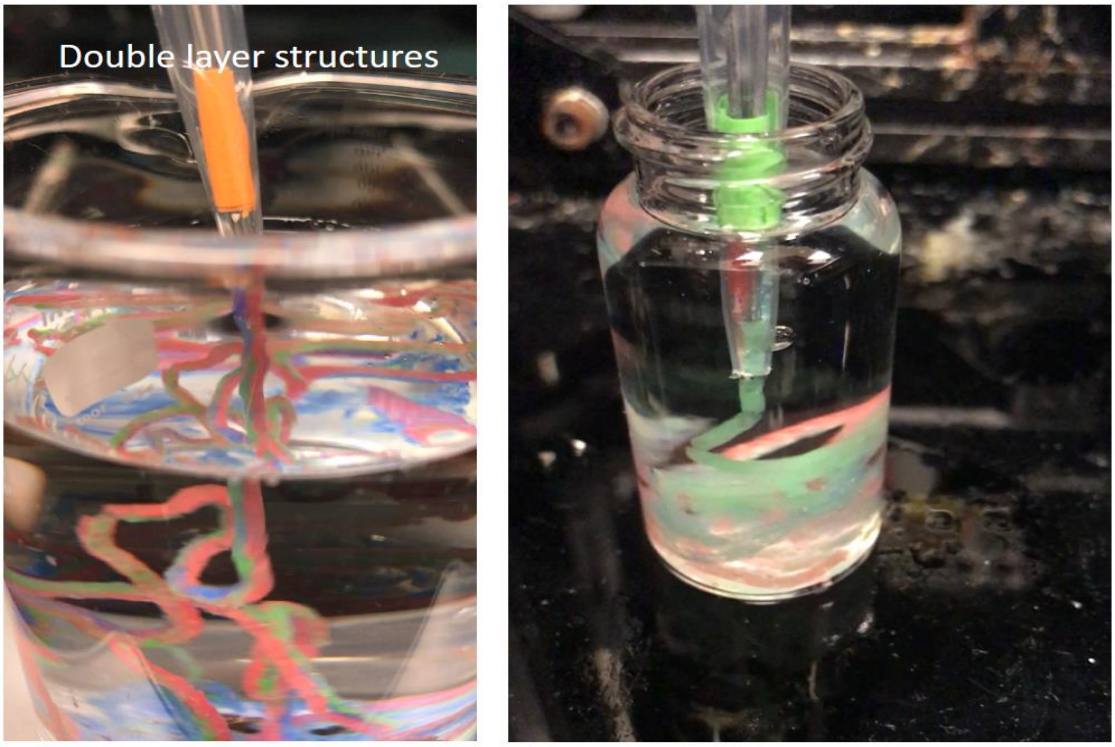

Figure 13: 3D printing of double and triple layer structures.
3D printing of double and triple layer structures of the shear-thinning gel using the multi-material extrusion bioprinter. 7NC50 (blue), 6NC50 (red) and 5NC50 (green) STBs were printed using the pressure ~40 kPa. The gels combined to form a single unified structure as it was extruded form the printer head. The low viscosity of 5NC50 gels lead to faster ejection of this gel.

Figure 14 shows the printing of 7NC50 (blue) and 6NC50 (red) STBs. The image shows that the silicate-based STB can be injected through the needle and form solid constructs after printing. Two different types of silicate-based STBs simultaneously injected through one single extrusion head and retained their structure even after injection. The scaffold also retained its structure when printed directly into liquid (Figure 12 and Figure 13). Figure 14(c) shows that the gel can be printed layer by layer and stacked. The thickness of the gel could be controlled by regulating the pressure used.

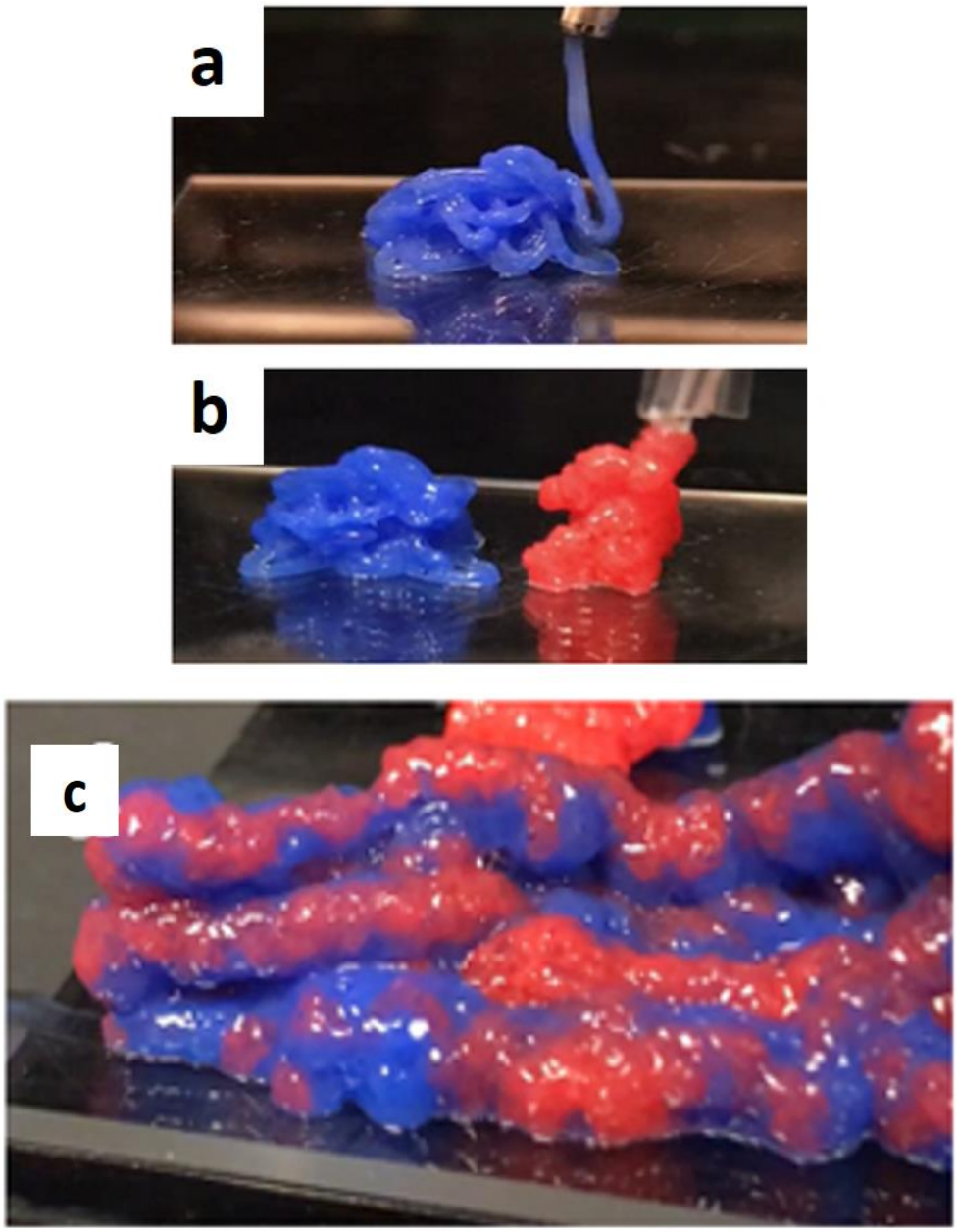

Figure 14: *3D printing of single and multi-layer structures.*
3D printing of single (a & b) and double-layer structures (c) of the shear-thinning gel using the multi-material extrusion bioprinter. 7NC50 (blue) and 6NC50 (red) STBs were printed using the pressure ~40 kPa.

After several trials, it was concluded that the gels in the range of 5-7 % solid content, with 50% silicate, had the best printing capability. The gels lower than 5% were too liquid and deformed easily once they were printed. Concentrations above 7NC75 were difficult to print, due to their high viscosity and required high pressure to print. Increasing the pressure of the printer would lead to leakage of the reservoirs or rapid ejection of the gel. Secondly, the high gas pressure also lead to formation of an empty hole through the reservoir, and pushed the

gel to the sides of the reservoir instead of through the needle opening. Taking these factors into account, the 7NC50 gels were chosen for the bone part and 6NC50 was chose to print the vessel part. Previous studies have shown that osteoblast cells proliferate better with higher silicate content [90]. Hence the higher concentration of silicate was chosen for the bone part. STBs were printed with a pressure off 35 – 40 kPa (~0,35 - 0,4 bar) for printing. This was advantages, as the printer uses one pressure for all outlets and uses this local pressure to print.

Visualization of STB interphase with fluorescent beads

Florescent beads were used to visualize the interphases between the different STB formulation when printed. Printed structure of 7NC50 (blue), 5NC50 (green) and 6NC50 (red) can be seen in Figure 15 (a). The structure was visualized under UV light. This construct was studied under the fluorescence microscope and the individual interphases between each STB can be seen in Figure 15 (b). The transition from one phase to the other can be clearly observed in these images. The gels are joined together, but not mixed.

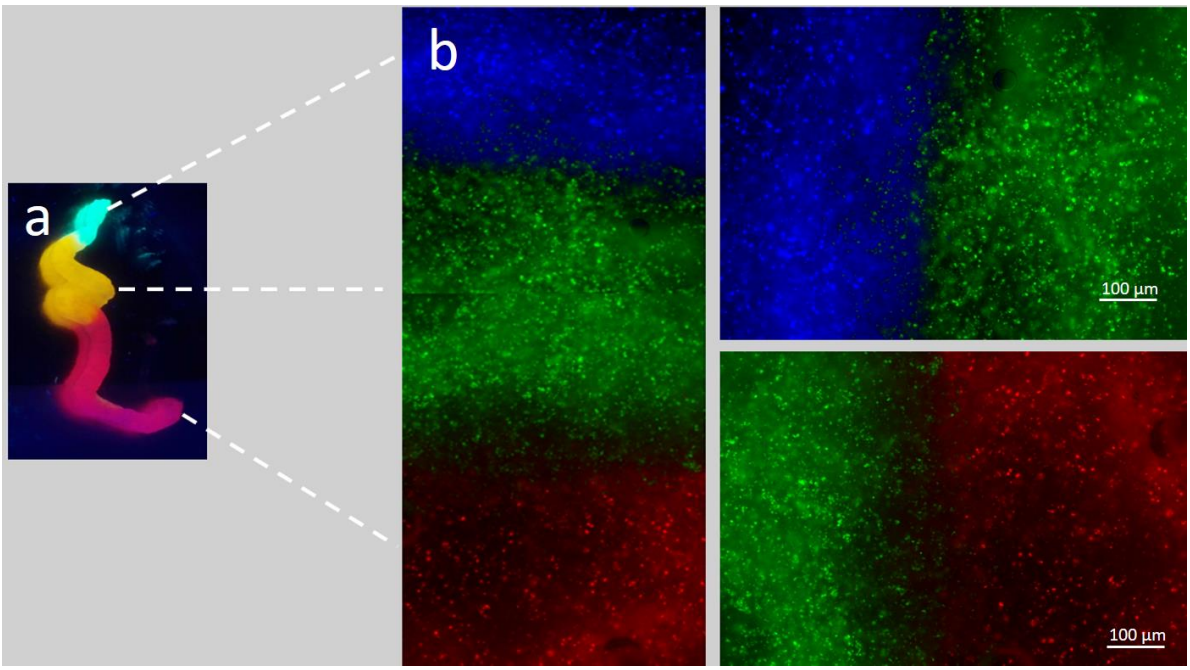

Figure 15: Visualization of STB interphase with fluorescent beads.

The gels with fluorescent beads, 7NC50 (blue), 6NC50 (red) and 5NC50 (green), were printed onto a glass slide and (a) visualized under the UV light. (b) Magnified images of the gel interphases were taken with the fluorescence microscope. The scale bar shows 100 µm. The particles were visualized under the fluorescence microscope using 100 x magnification.

3.1.3 Injectability of shear-thinning gel with different sizes of PCL nanoparticles

Injection force measurement was performed using Instron mechanical tester to evaluate how PCL particles and STB formulations effected the injectability of the gel. The results are seen in Figure 16. The increase in particle size caused the gel to have higher viscosity, due to which it is difficult to inject and thus need higher injection force. All gels were injected through 18-gauge syringe needles. It was observed that, the larger the PCL particles was, the harder it was to inject.

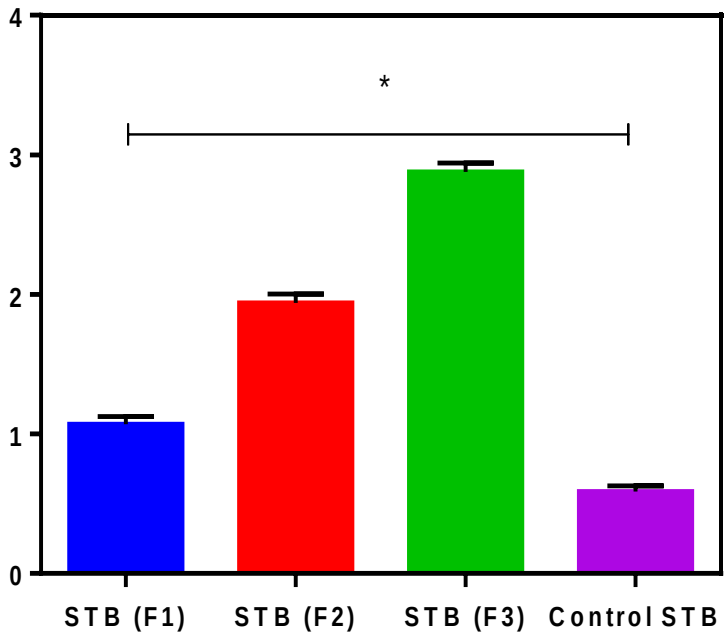

Figure 16: Injection force test of STB/PCL combinations with Instron.
The injection force required to eject, 7NC50 and 6NC50 gels were tested with F1, F2 and F3 particles. Gels with no particles served as controls. Higher injection force was needed with larger sized particles. Lower solid content of the gel, lead to lower injection force measurements. Data shown are mean values ± SD of n = 3 of a single experiment. *P* values determined by one-way ANOVA followed by Tukey post hoc comparison (*$p < 0.05$).

3.1.4 Rheological characterization of STB

Figure 17 shows the strain dependent oscillatory shear-rheology of the STB formulations, with and without PCL particles. The Storage moduli (G′) of STBs was measured to evaluate the strength of the gels. The strain dependent oscillatory rheology of the gels showed that, the shear storage modulus (*G'*) increased with more solid content and addition of PCL

particles. The results show that the gels had a broad linear viscoelastic region, showing ideal shear-thinning behavior of the gels.

G′ ↑: PCL & ↑ silicate%

Figure 17 shows the strain sweep of STBs. In the case of 6NC50 gels, the gel disrupts is at ~10% strain. Below 10% strain, the structure is intact, the material retains its solid like behavior. The critical strain is the point at which the storage modulus starts to drop. Increasing the strain above the critical strain disrupts the network structure.

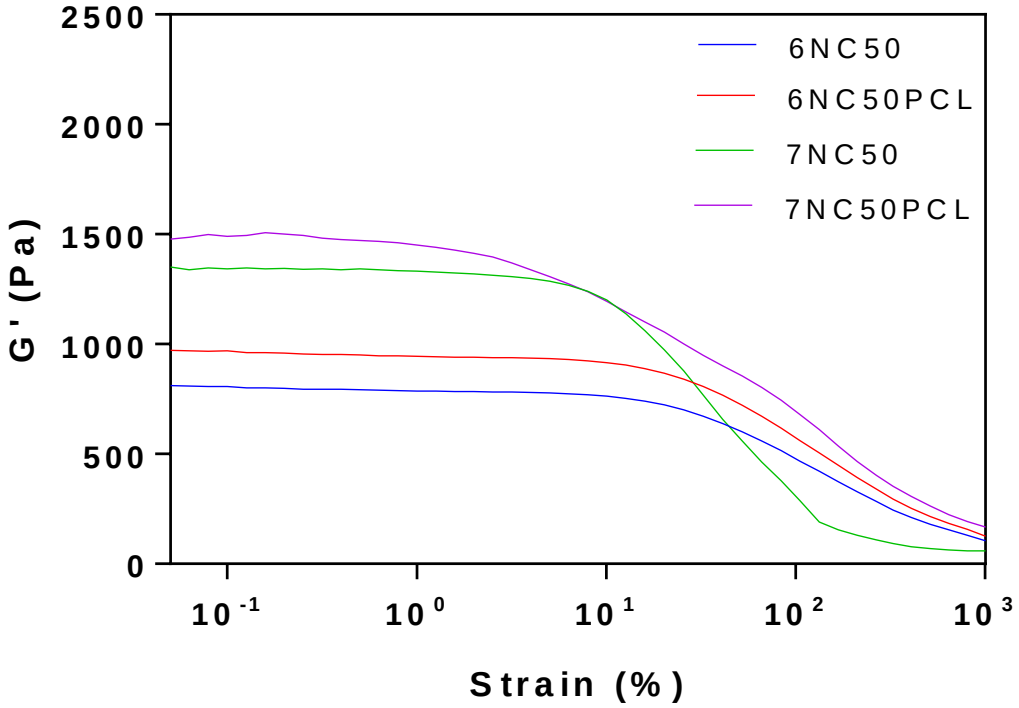

Figure 17: The effect of increasing strain on the storage modulus (G') different STG/PCL formulations. Dynamic strain sweep test was conducted, during which an increasing strain, ranging from 0.1-1000 %, was applied to the STBs (6 rad/s). A constant temperature of 37 °C was maintained during the measurement. Shear storage modulus (G′) increased with increasing solid content and addition of PCL particles. All gels displayed a broad linear viscoelastic region, indicating good shear-thinning behavior.

Dynamic time sweep was performed with different STBs to measure the time-dependent progress of storage (G′) moduli. First a steady shear flow was applied to disrupt the gel. Once the shear flow was stopped, repair of gel rigidity was instantly observed over time in a subsequent dynamic time sweep. The recovery data of all gels are shown in Figure 18 - Figure 23. Good self-healing property of the gels was observed. The self-healing property

allows the gels to flow under applied shear stress and enables them to recover and regain their mechanical properties, when the stress is released.

Figure 18 shows the self-healing behavior of 3,75NC75 gels with and without PCL. The storage modulus of 1000 Pa is observed at the starting of the experiment. When high strain is applied the storage modulus drops to ~5 - 10%. When the stain is removed, the gel recovers and reaches its original G', even after 4 rounds of alternation strain is applied.

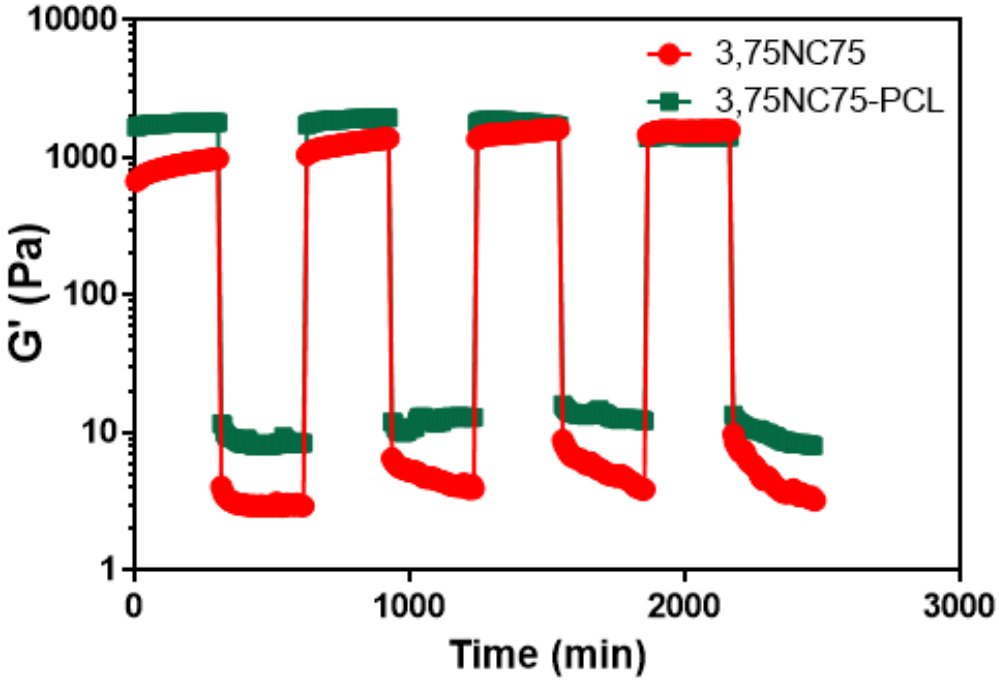

Figure 18: Self-healing behavior of 3,75NC75 STB with and without PCL.
The storage moduli (G') of STBs after repeated application of high strain 100% strain followed by 1% strain for 5 min, to monitor gel recovery is seen. Fast recovery of the storage modulus after application of oscillatory strain amplitudes.

Figure 19 shows the self-healing behavior of 4,5NC50 gels with and without PCL. The storage modulus of ~200 - 250 Pa is observed at the starting of the experiment. When high strain is applied the storage modulus drops to ~20 - 50%. When the stain is removed, the gel recovers and reaches its original G', even after 4 rounds of alternation strain is applied.

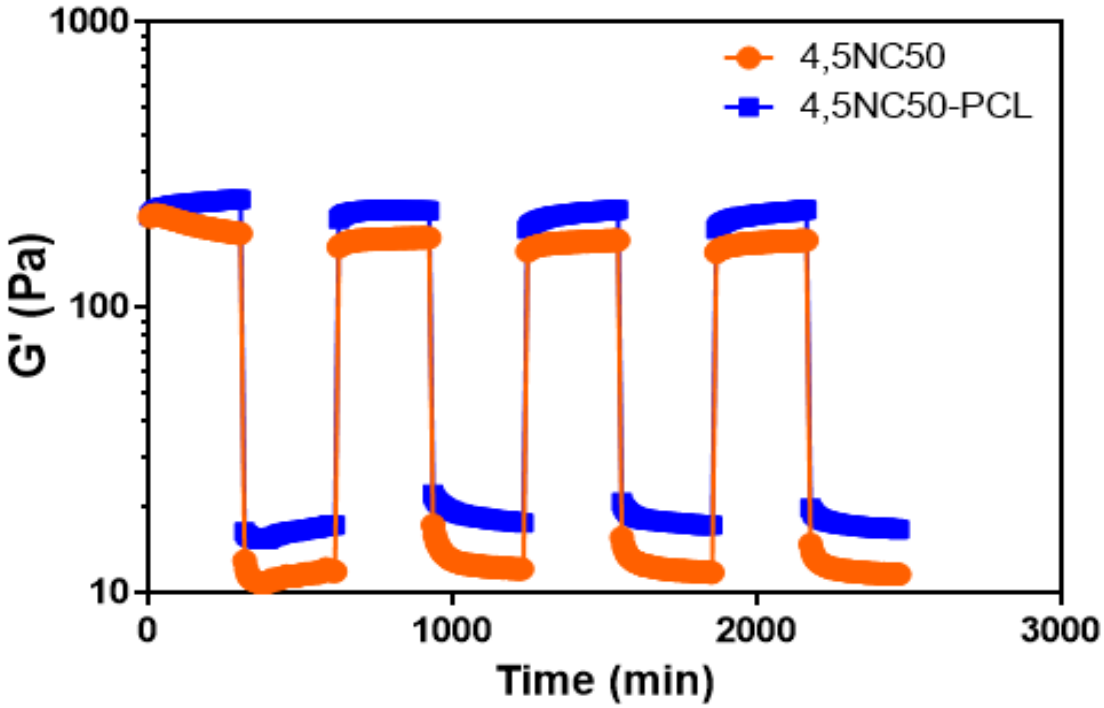

Figure 19: Self-healing behavior of 4,5NC50 STB with and without PCL.
The storage moduli (G') of STBs after repeated application of high strain 100% strain followed by 1% strain for 5 min, to monitor gel recovery is seen. Fast recovery of the storage modulus after application of oscillatory strain amplitudes.

Figure 20 shows the self-healing behavior of 5NC50 and 5NC75 gels with and without PCL. 5NC70 with PCL showed the highest storage modulus of ~1856 Pa. However, the storage modulus dropped to 675 Pa after 4 cycles. This could be due to improper preparation or loading of the sample.

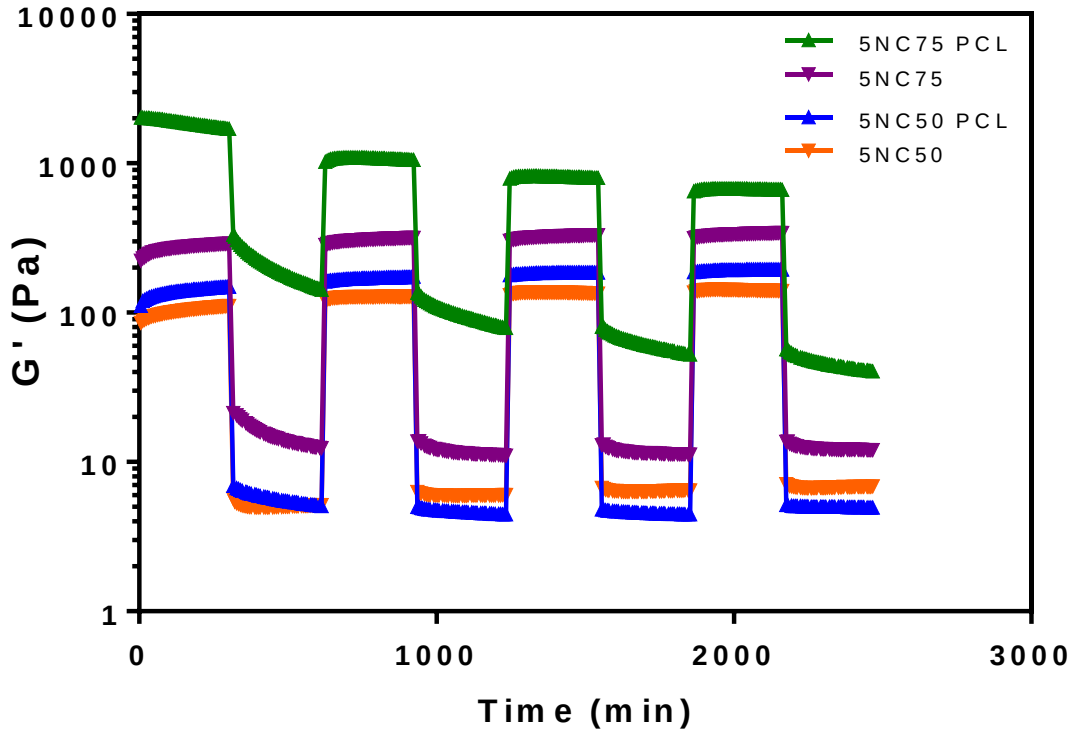

Figure 20: Self-healing behavior of 5NC50 and 5NC75 STB with and without PCL.
The storage moduli (G') of STBs after repeated application of high strain 100% strain followed by 1% strain for 5 min, to monitor gel recovery is seen. Fast recovery of the storage modulus after application of oscillatory strain amplitudes. The data for 5NC70 is irregular, with high storage modulus at the beginning. This drops to 675 Pa after the end of 4 cycles.

Figure 21 shows the self-healing behavior of *6NC50 and 6NC75 STB* with and without PCL. *6NC75 STB* with and without PCL with higher silicate content has higher storage modulus of ~1500 Pa which increases slightly after the 4 cycles. The increase in storage modulus in STB formulations could be due to variations in STB preparation or loading errors (e.g. bubbles in sample).

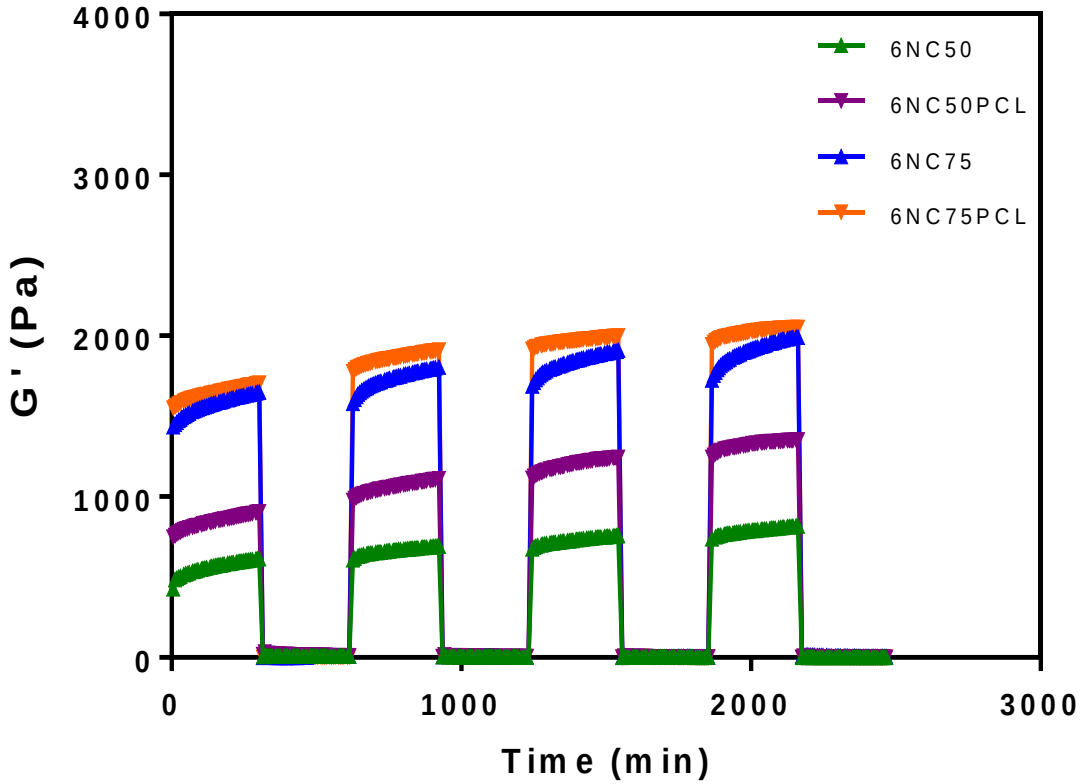

Figure 21: Self-healing behavior of 6NC50 and 6NC75 STB with and without PCL.
The storage moduli (G′) of STBs after repeated application of high strain 100% strain followed by 1% strain for 5 min, to monitor gel recovery is seen. Fast recovery of the storage modulus after application of oscillatory strain amplitudes.

Figure 22 shows the self-healing behavior of 7NC50 and 7NC75 STB with and without PCL. 7NC75 STB with PCL and higher silicate content has the highest storage modulus of ~2000 Pa which increases slightly after the 4 cycles. The increase in storage modulus in STB formulations could be due to variations in STB preparation or loading errors (e.g. bubbles in sample). 7NC50 STB with PCL has the most constant G' measurement. This gel reaches its original G', even after 4 rounds of alternation strain application.

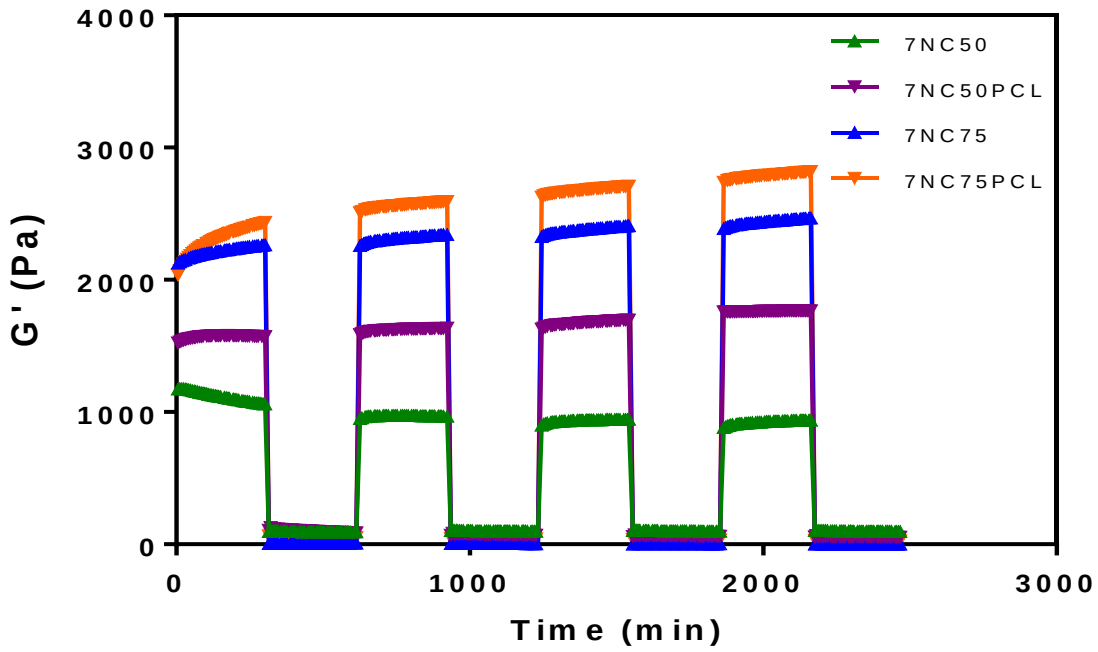

Figure 22: Self-healing behavior of 7NC50 and 7NC75 STB with and without PCL.
The storage moduli (G′) of STBs after repeated application of high strain 100% strain followed by 1% strain for 5 min, to monitor gel recovery is seen. Fast recovery of the storage modulus after application of oscillatory strain amplitudes.

Figure 23 shows the storage modulus of 6NC and 7NC gels with and without PCL. The addition of PCL particles enhanced the mechanical properties of silicate gels. The mechanical strength of the gel increases with increased silicate content and PCL.

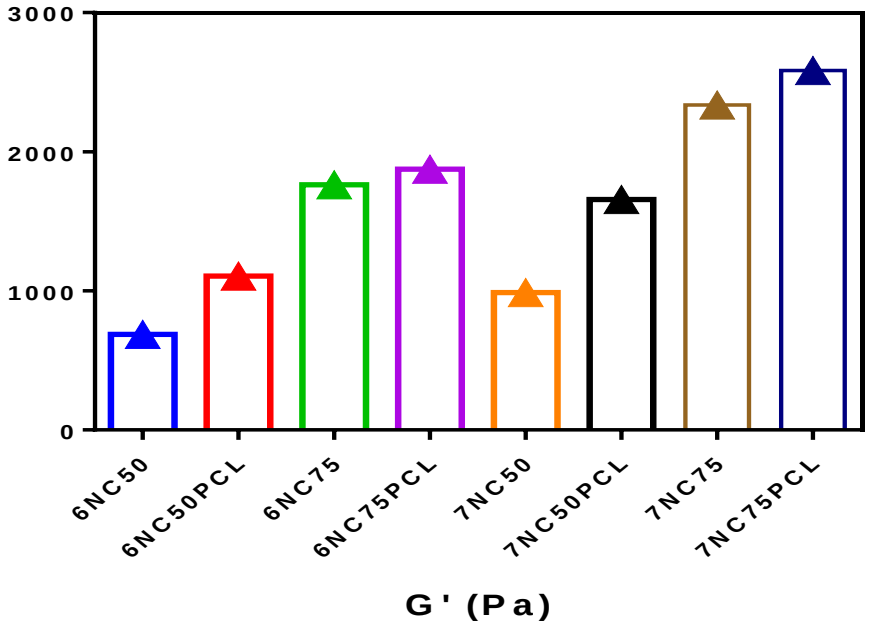

Figure 23: Storage modulus of 6NC and 7NC gels with and without PCL.
The data is shown using a scatter plot. The amount of silicate and the presence of PCL influences the mechanical strength of the STB.

3.2 Biocompatibility of Shear-thinning nanocomposite with PCL nanoparticles

In vitro analysis of cell seeded in scaffold was done to assess the compatibility of the scaffold. Preliminary experiments were performed with only osteoblast seeded in STB to set the ideal parameters for staining (images not shown).

The experiments were performed with empty PCL particles before doing the main experiment with VEGF loaded particles. The cell/scaffolds were cultured for 7 days. The osteoblasts were seeded in 7NC50 STB and the endothelial cells in the 6NC50. Empty PCL particles without any encapsulates, were used for this experiment to study the effect of PCL nanocapsules on cell proliferation and viability. The staining images (see *Figure 24* - *Figure 28*) showed that the PCL had no cytotoxic effect on the co-cultured cells. All groups with and without PCL have high viability.

The mechanical tests could show that the addition of PCL particles greatly improved the mechanical strength of the STBs. However, the live/dead staining of the cells helped evaluate if the PCL had any influences on cell viability. However, since no cell specific stainings were performed, the viability of the two cell types cannot be disguised. No brightfield images of the stainings were acquired, as these images were not clear due to the thickness of the gels.

Figure 24 - Figure 28 show that the cell viability was high, even when PCL particles were present in the gel. There is no increase is viability detected due to PCL particles. The particles seem to have very little to no effect on the survival of the cells.

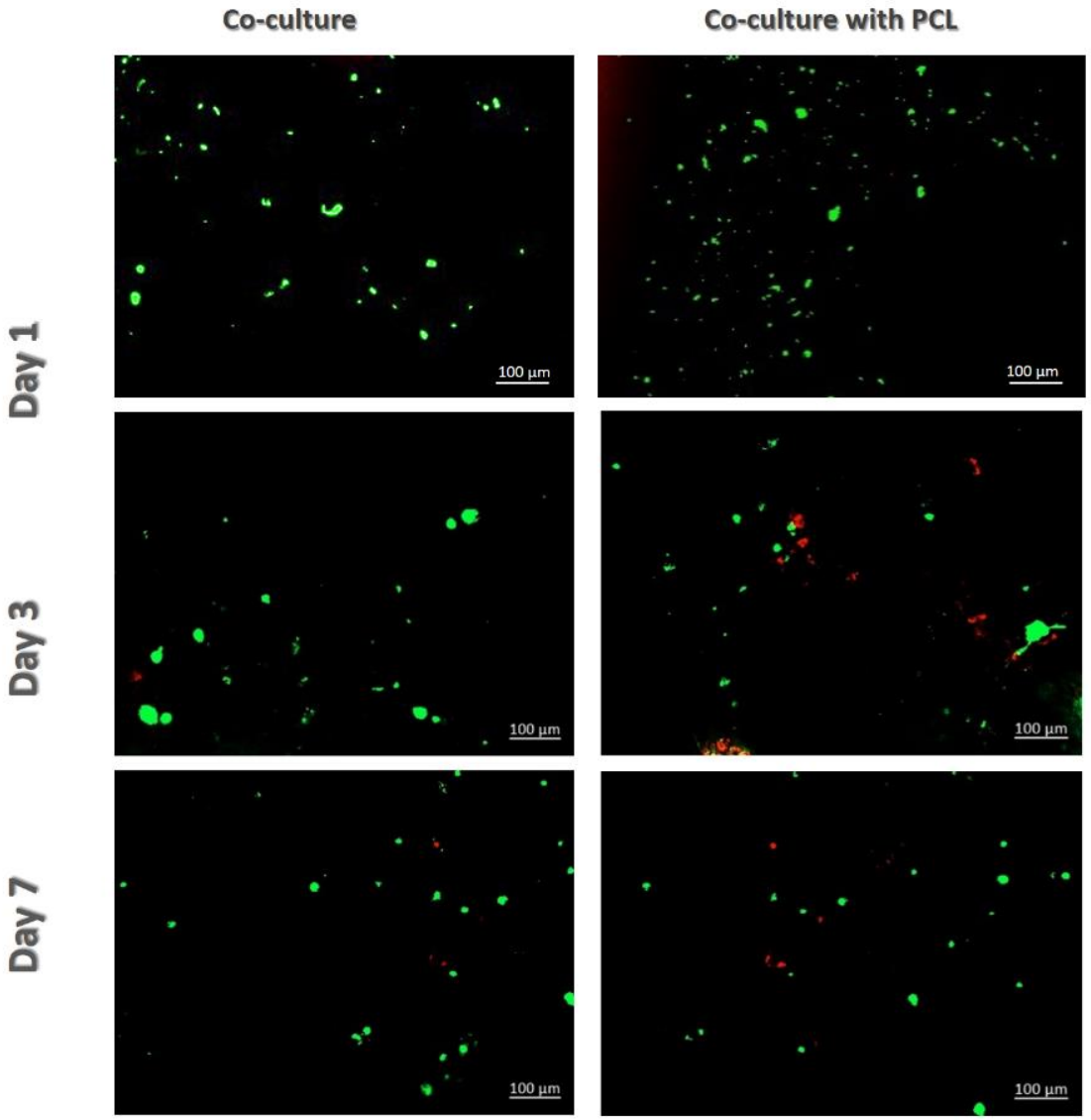

Figure 24: Calcein AM/ethidium homodimer-1 staining of co-culture cells with/without PCL.
Live/dead staining of gels with osteoblasts seeded in 7NC50 STB and the endothelial cells in the 6NC50 (day 1, 3 and 7). Viability of over 90% can be observed in all images (green fluorescence). Images acquired at 100x magnification.

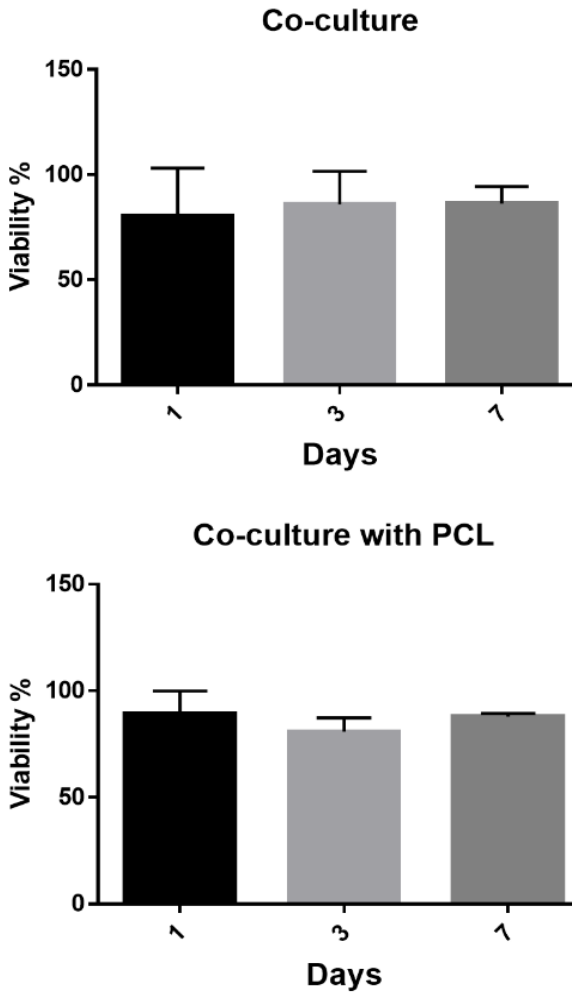

Figure 25: Viability of co-culture cells with/without PCL.
Live/dead staining of gels with osteoblasts seeded in 7NC50 STB and the endothelial cells in the 6NC50 (day 1, 3 and 7) were performed and the viability calculated based on this equation: Viability = (live/ live + Dead) *100. Data shown are mean values + SD of a single experiment measured in triplicates.

Figure 26 shows that the cell viability was high, even when PCL particles were present in the gel. There is no increase is viability detected due to PCL particles. However, a lower viability of ~75% was observed in osteoblasts cultured with PCL on day 1. These cells later recovered and showed much higher viability on day 7 of culture.

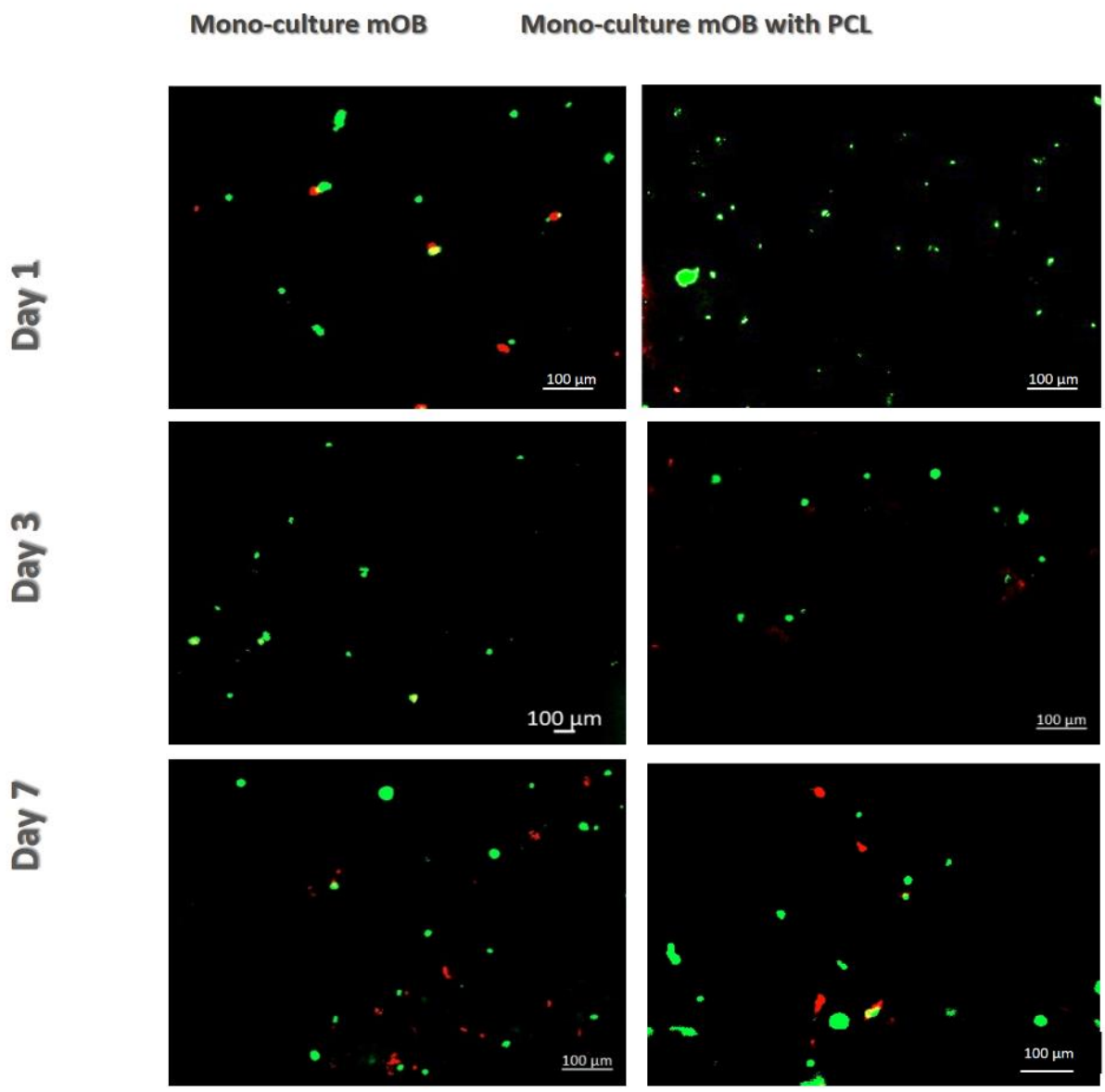

Figure 26: Calcein AM/ethidium homodimer-1 staining of mono-culture osteoblast cells with/without PCL.

Live/dead staining of gels with osteoblasts seeded in 7NC50 STB (day 1, 3 and 7). Images acquired at 100x magnification. Viability of almost 90% can be observed in all groups, apart from osteoblasts cultured with PCL on day 1 (~75% viability).

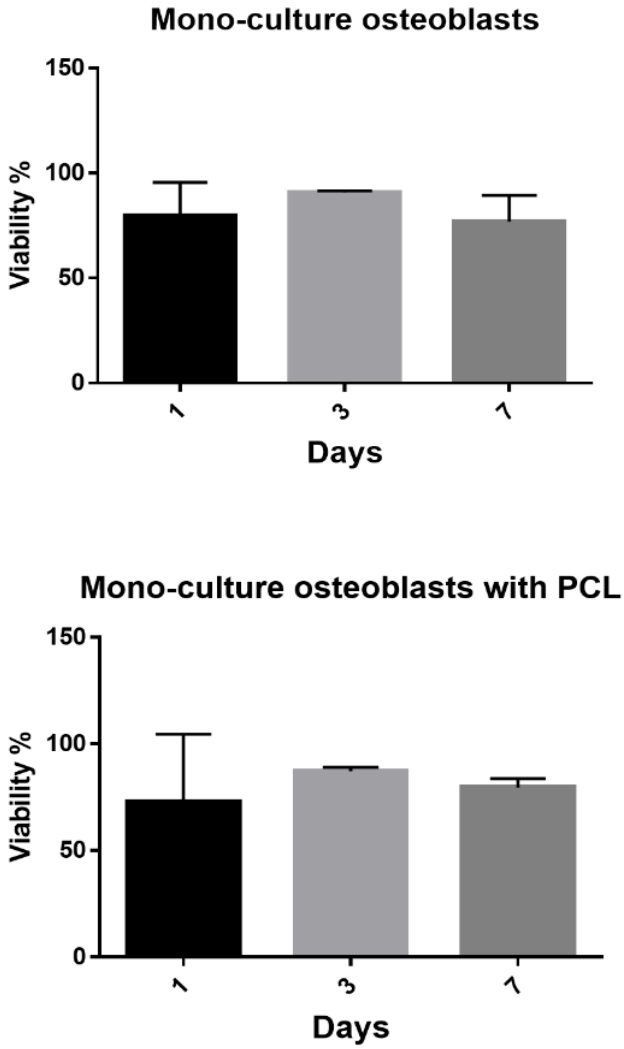

Figure 27: *Viability of mono-culture osteoblast cells with/without PCL.*
Live/dead staining of gels with osteoblasts seeded in 7NC50 STB were performed and the viability calculated based on this equation: Viability = (live/ live + Dead) *100. Data shown are mean values + SD of a single experiment measured in triplicates.

Figure 28 shows that the cell viability was high, even when PCL particles were present in the gel, except for endothelial cells with PCL on day 1. These cells had a very low viability of ~50% at the start of culture. The underlying reason for this initial incompatibility to PCL particles would need to be further investigated.

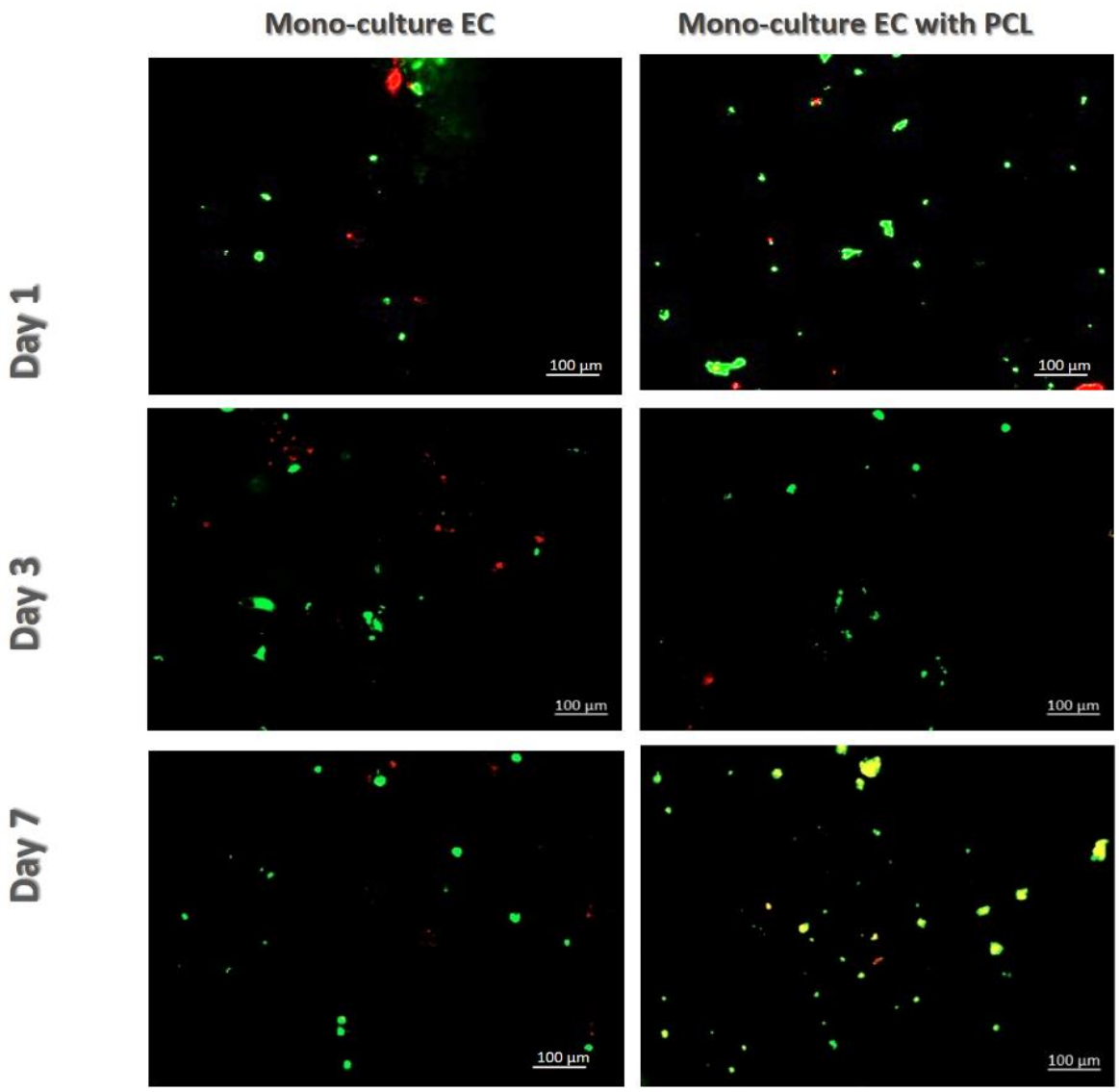

Figure 28: Calcein AM/ethidium homodimer-1 staining of mono-culture endothelial cells with/without PCL.

Live/dead staining of gels with endothelial cells seeded in 6NC50 STB (day 1, 3 and 7). Viability of almost 90% can be observed in all images (green fluorescence). However, the viability graph shows that the endothelial cells with PCL had an initial fall in cell viability on day, which they recovered from till day 7. Images acquired at 100x magnification. Live/ Dead images show that that the addition of PCL beads in STB can improve mechanical strength without altering cell viability.

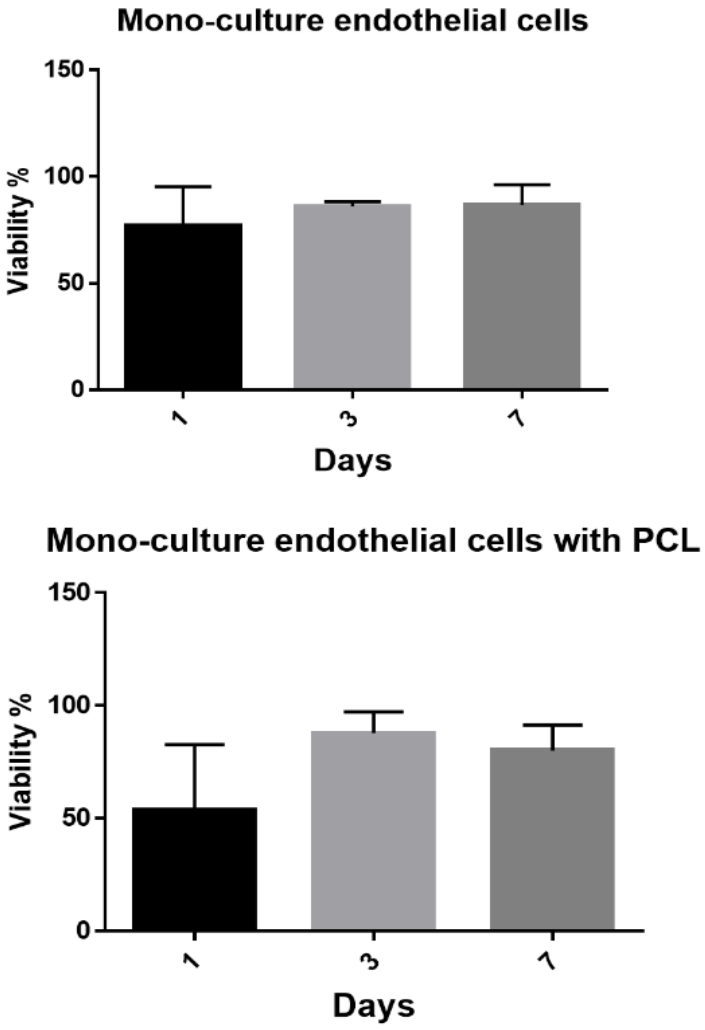

Figure 29: Viability of mono-culture endothelial cells with/without PCL.
Live/dead staining of gels with endothelial cells in the 6NC50 (day 1, 3 and 7) were performed and the viability calculated based on this equation: Viability = (live/ live + Dead) *100. Data shown are mean values + SD of a single experiment measured in triplicates.

PrestoBlue assay is reliant on the metabolic activity in cells. It helps measure the cells metabolic activity of the cells by colorimetric method. This method is easy to use and has a high reproducibility, due to which it was performed in addition to CalceinAM/*ethidium homodimer-1* staining [13], [14]. Figure 30 shows how the addition of PCL particles effects the proliferation of the cells. The graphs show that PCL had a positive effect of proliferation, especially in the case of co-cultured cells. By comparison of the 2 groups, it is also seen that the co-culture of the cells lead to an increase in cell growth on day 3. However, it was seen that the proliferation of co-cultured cells had decreased by 16.8% from day 3 to day 7. Whereas, when the cells were co-cultured in the presence of PCL, there was a 31.8% increase in proliferation from day 3 to day 7. It was observed that the proliferation of monocultured osteoblast dropped by a significant amount from day 1 to 7. This was also

seen in mono-cultured endothelial cells. Further tests would have to be performed to evaluate the reasons behind the decline in proliferation of these cells. The results suggest that the outcomes of the live/dead stainings do no completely correlate with what was observed from the PrestoBlue assay results.

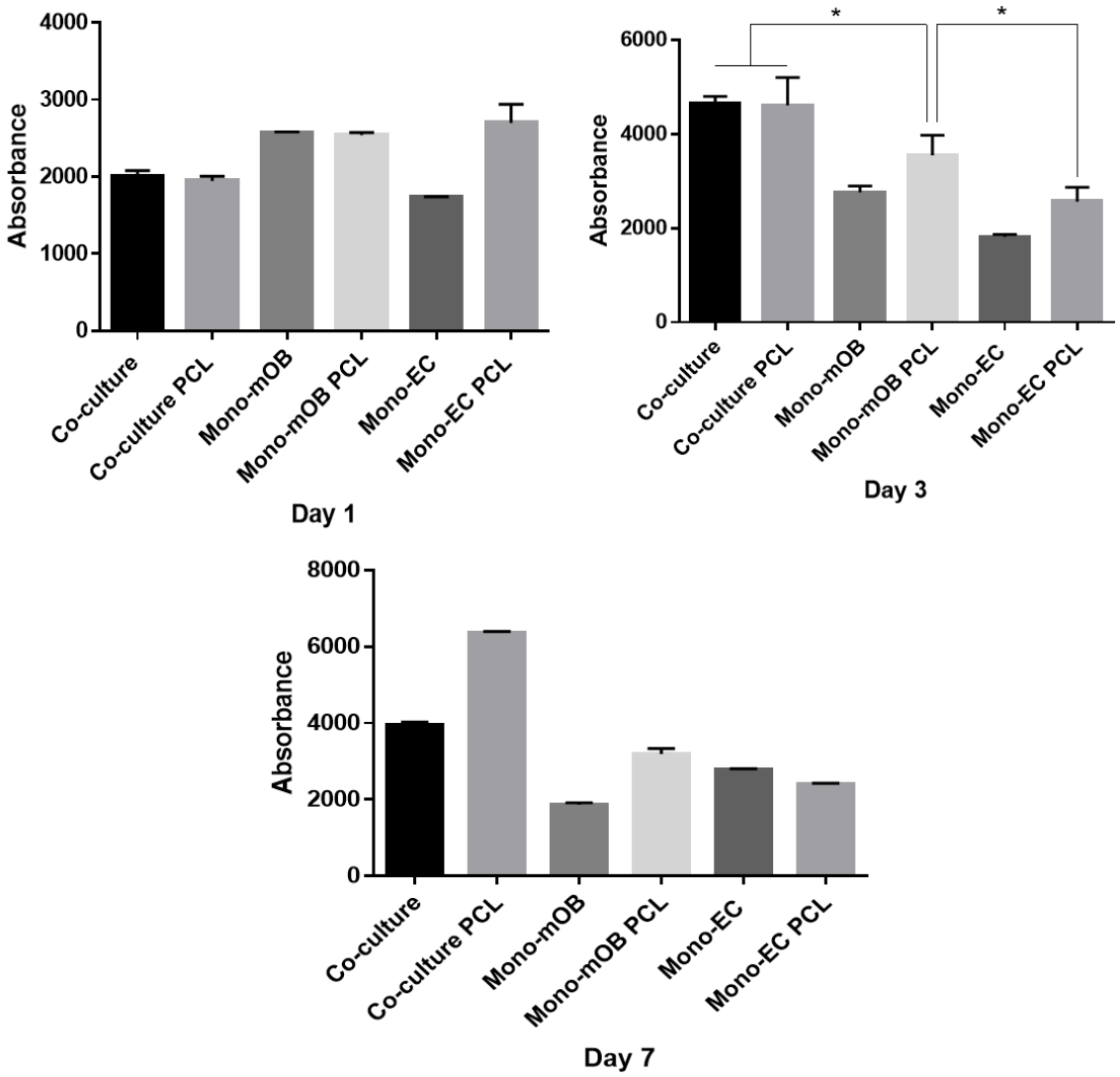

Figure 30: Proliferation of cells seeded in STB with/without empty PCL, measured using PrestoBlue assay.

The presence of PCL had positive effect on co-cultured cells and had a 3-fold increase in just 7 days. The mono-culture of endothelial cells showed a decrease in proliferation in the cells cultured with PCL particles. Both endothelial cells and osteoblasts showed decreased proliferation over time. Data shown are mean values + SD of n = 3 of a single experiment. *P* values determined by two-way ANOVA followed by Tukey post hoc comparison (*p < 0.05).

Figure 31 shows the PrestoBlue assay results of the *in vitro* compatibility experiment using VEGF loaded PCL particles. The results showed that the addition of VEGF loaded PCL particles had a positive effect of proliferation, except for in mono-culture with osteoblasts.

This is clearly observed on day 7, where the osteoblast cultured with PCL seem to have much lower proliferation rate than the cells without PCL. Further studies will have to be performed to evaluate the underlying reasons to why the PCL particles had a negative effect on the osteoblasts. The co-culture and monoculture endothelial cells had higher proliferation with the addition of the growth factor loaded particles. Comparing the co-culture samples on day 7, there was a 14.8% higher cell proliferation in the group that had VEGF loaded particles. The higher proliferation on co-cultured cells could be due to the complimentary effect both the cells have on each other.

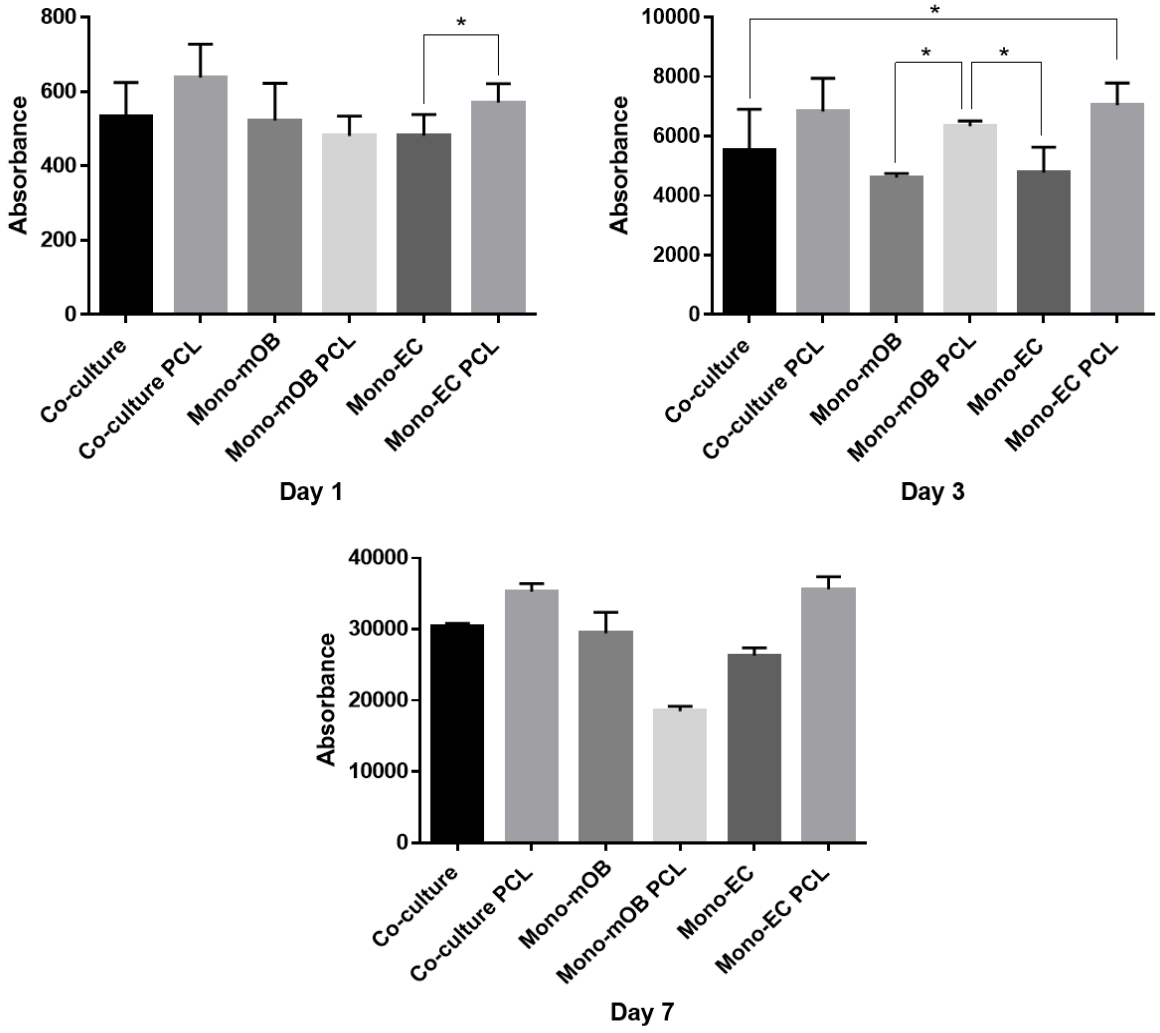

Figure 31: Proliferation of cells seeded in STB with/without VEGF loaded PCL, measured using PrestoBlue assay.

The presence of PCL had a positive effect on co-cultured cells and mono-cultured of endothelial cells. The presence of PCL had a negative effect of the proliferation of osteoblasts cells on day 1 and day 7. The co-culture of cells and mono-culture of endothelial cells had a positive proliferation growth from day 1-7, which was improved by the presence of PCL. Data shown are mean values + SD of n = 3 of a single experiment. *P* values determined by two-way ANOVA followed by Tukey post hoc comparison (*$p < 0.05$).

3.3 Actin/DAPI staining of osteoblasts seeded in 7NC50 STB

To visualize the structure of the cytoskeleton, osteoblast seeded in 7NC50 gel were stained with Actin/DAPI (see Figure 32). The images show unspecific staining of Actin (green). It was also observed that the cells were not distributed evenly throughout the scaffold (blue DAPI staining of the nucleus), which could have been due to inadequate mixing of the cells in the scaffold while seeding. The cell seeding density seems to be very low (2 million cells/ml gel).

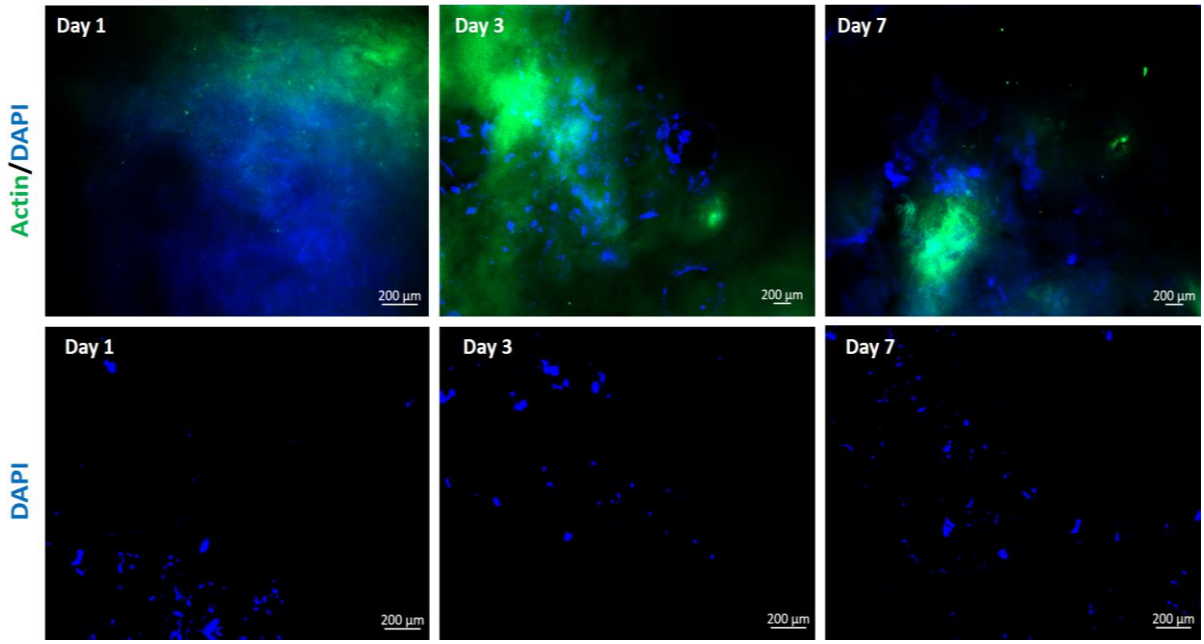

Figure 32: Actin/DAPI staining of osteoblast in 7NC50 gel.

The positive nuclear staining for DAPI (blue) can be observed in all images and shows very few cells distributed unevenly throughout the scaffold. Actin staining (labelled with green-fluorescent Alexa Fluor® 488 dye) is extremely unspecific with high background staining. Images acquired at 100x magnification.

This experiment was not repeated.

3.4 Cell tracker analysis

Since both live/dead staining and presto blue assay could not differentiate between the osteoblast and endothelial cells, an additional live cell tracking analysis was performed to identify each of the respective cell types during 21 days of culture in STB with and without PCL. Osteoblast cells were labeled with green cell tracker and endothelial cells were labeled with red tracker. Figure 33 - Figure 36 show the cell tracker images from day 1-7 of culture. Osteoblasts were seeded in 7NC50 STB and treated with green cell tracker. The endothelial cells were seeded in the 6NC50 and treated with red cell tracker. From the images, there is no significant difference seen in the growth of the cells with/without PCL. There is clear increase in proliferation of the cells in the 7 days of culture. No brightfield images were acquired due to poor image quality caused by scaffold thickness.

Figure 33 shows the cell tracker images of co-cultured cells on day 1. No osteoblasts (green) were seen in STB without PCL at this timepoint. This however, could have been due to improper settings of the microscope. The only image with both osteoblast (green) and endothelial cells (red) were acquired on day 1. It was difficult to focus both florescence channels at the same time. This could have been overcome with better microscope settings.

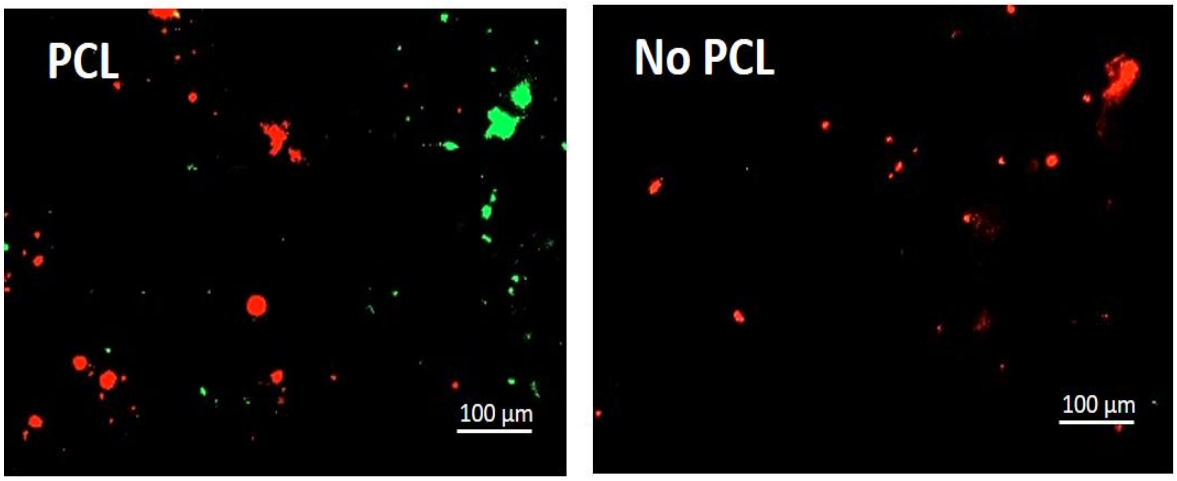

Figure 33: Cell tracker analysis to identify osteoblast and endothelial cells seeded in STB with and without PCL on day 1.

Cells were stained with cell tracker and then encapsulated in STB. Osteoblasts (green) were seeded in 7NC50 STB and endothelial cells (red) in 6NC50. Cell tracker was added to the cells before culture to visualize and distinguish the growth of the 2 different cell types in co-culture experiment. Images were acquired at 100x magnification.

Figure 34 shows images of the cell tracker analysis on day 3 of culture. No images with both cell types were acquired at this timepoint. Proliferation of both cell types have improved since day 1 and many cells are seen homogenously distributed throughout the scaffold.

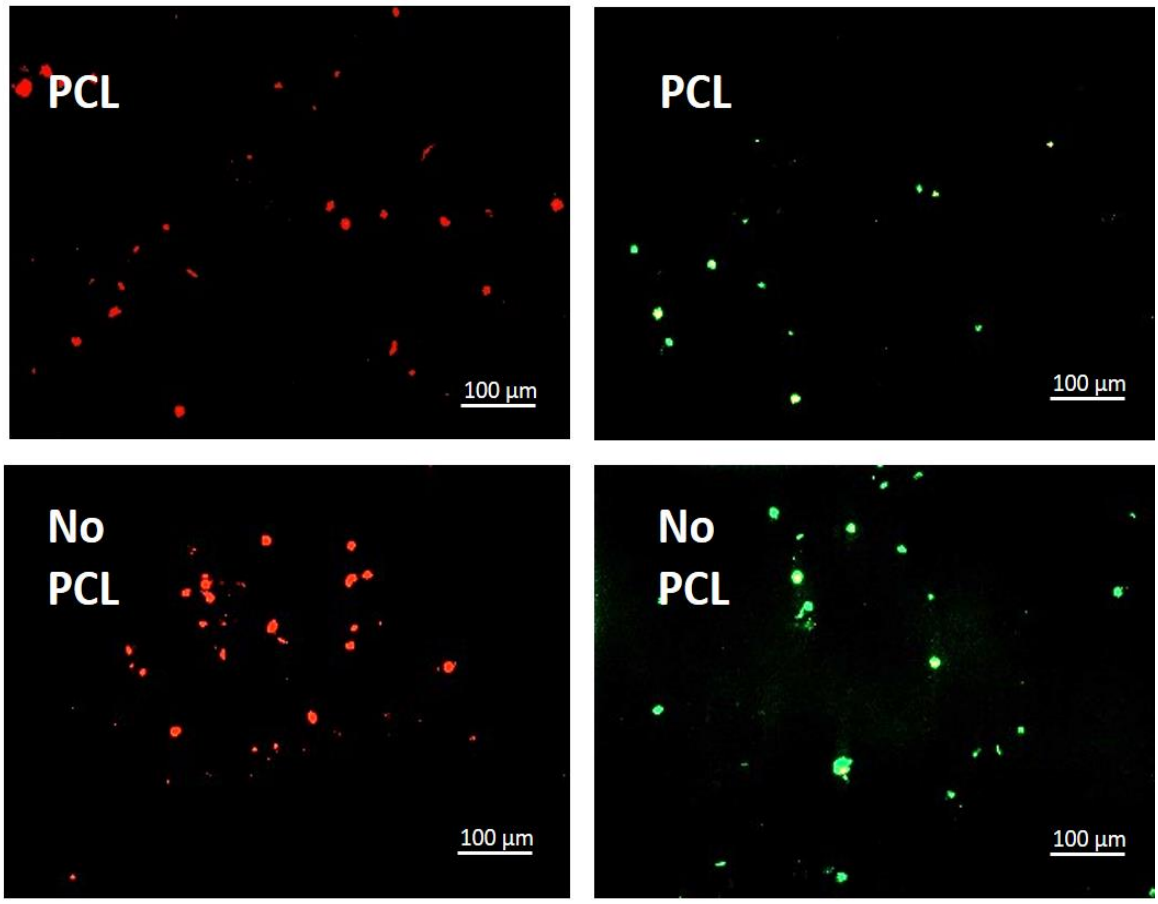

Figure 34: Cell tracker analysis to identify osteoblast and endothelial cells seeded in STB with and without PCL on day 3.
Cells were stained with cell tracker and then encapsulated in STB. Osteoblasts (green) were seeded in 7NC50 STB and endothelial cells (red) in 6NC50. Cell tracker was added to the cells before culture to visualize and distinguish the growth of the 2 different cell types in co-culture experiment. Images were acquired at 100x magnification.

Figure 35 shows images of the cell tracker analysis on day 7 of culture. No images with both cell types were acquired at this timepoint. Proliferation of both cell types have improved since day 1 and many cells are seen homogenously distributed throughout the scaffold. There is a slight increase in cell number observed, in endothelial cells (red). PCL particles do not seem to have had a negative effect on the proliferation of endothelial cells. The osteoblasts (green) seem to be proliferating much slower than the endothelial cells.

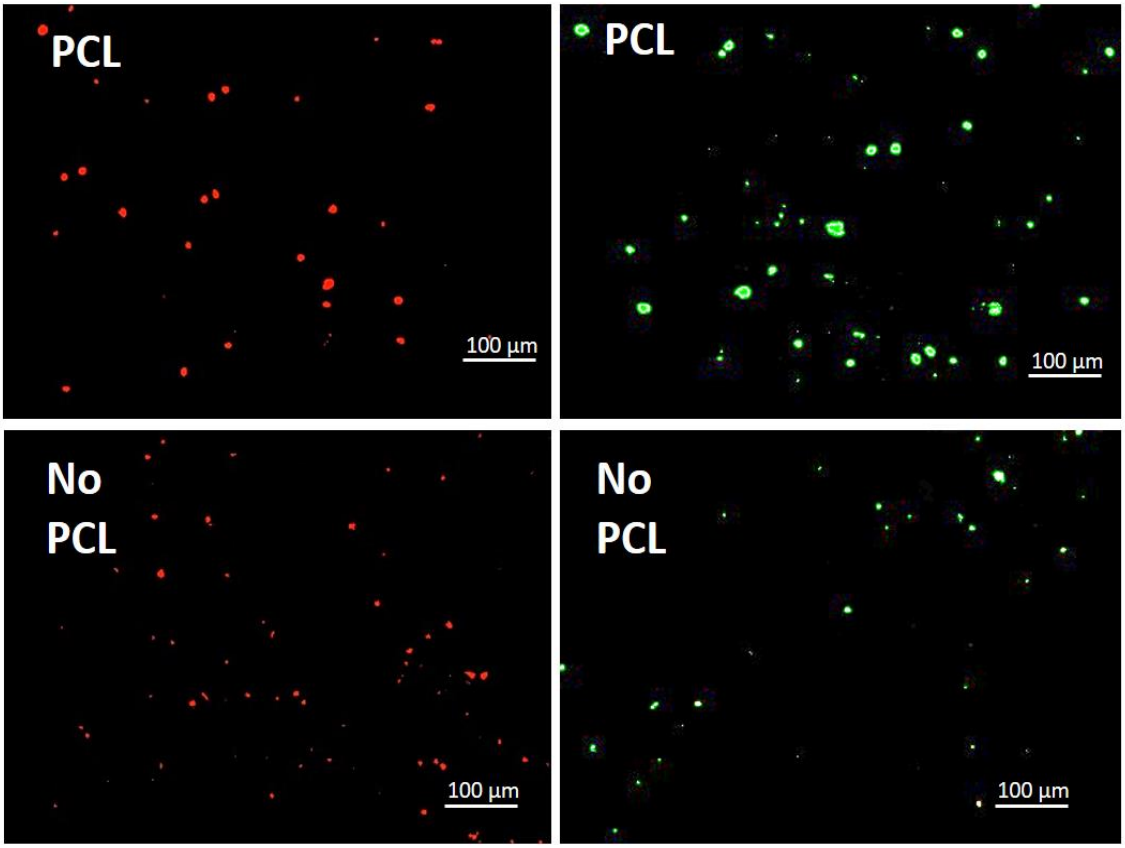

Figure 35: Cell tracker analysis to identify osteoblast and endothelial cells seeded in STB with and without PCL on day 7.

Cells were stained with cell tracker and then encapsulated in STB. Osteoblasts (green) were seeded in 7NC50 STB and endothelial cells (red) in 6NC50. Cell tracker was added to the cells before culture to visualize and distinguish the growth of the 2 different cell types in co-culture experiment. Images were acquired at 100x magnification.

Figure 36 shows images of the cell tracker analysis on day 21 of culture. No images with both cell types were acquired at this timepoint. Proliferation of endothelial cells (red) have improved, especial for cell with PCL. However, the number of osteoblasts (green) seem to have decreased. This result correlates with PrestoBlue results previously acquired, where the osteoblast showed low proliferation in STB.

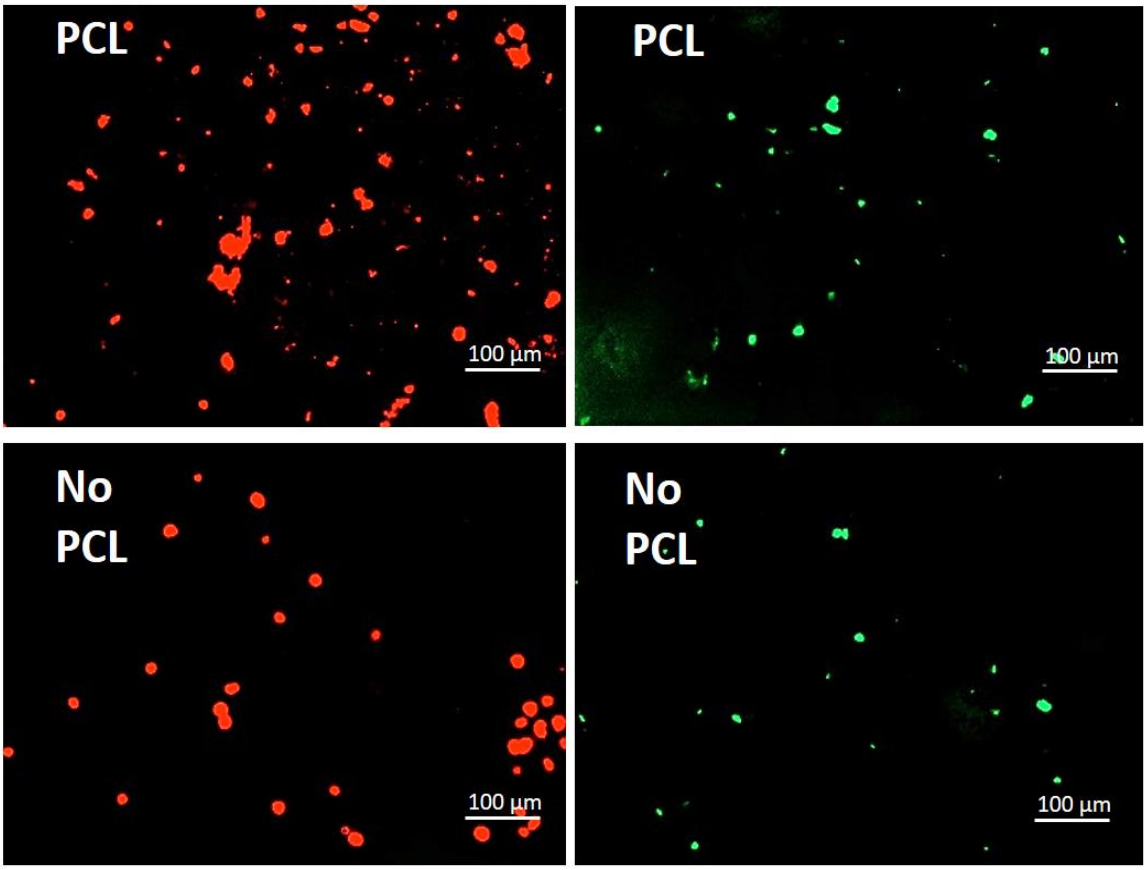

Figure 36: Cell tracker analysis to identify osteoblast and endothelial cells seeded in STB with and without PCL on day 21.

Cells were stained with cell tracker and then encapsulated in STB. Osteoblasts (green) were seeded in 7NC50 STB and endothelial cells (red) in 6NC50. Cell tracker was added to the cells before culture to visualize and distinguish the growth of the 2 different cell types in co-culture experiment. On day 21 endothelial cells showed high proliferation. However, a low concentration of osteoblasts was seen at this timepoint. Images were acquired at 100x magnification.

4 Discussion

In spite of current advances in the field of bone tissue engineering, a suitable treatment for nonunion fracture still does not exist. Even with successful generation of organic and inorganic materials that have similar physicochemical properties with bone, engineering vascularized bone implant materials are still in their starting stage. [9, 27, 33]. Autologous and allogenic transplants are very commonly used in clinical practice. However, as already explained, these have many limitations. Most bone implant materials today are composed of inorganic bone materials (e.g. calcium phosphate). These materials have high densities and produce a lot of heat during the curing process. This makes them unsuitable as active cell and growth factor carries [26, 83]. Although there have been several encouraging studies for developing vascularized bone implant materials, most of them are still not ready for clinical use. This is mainly due to the difficulty of regulating multiple tissue types and the complexity of pre-establishing peripheral vascular networks in bone grafts before implantation [27, 70].

Silicate and gelatin-based STBs have been previously tested in *in vitro* and *in vivo* studies and have shown to be useful for the treatment of hemorrhage and endovascular embolization [84, 95]. Gelatin, which is denatured collagen can partially mimic the native extracellular matrix components of native bone tissue. Gelatin and silicate interaction can lead to the formation of cross-linked networks, which can rapidly form and deform under pressure. This is known to be enabled by stark attractive interaction potential between the materials, which causes distinct binding of the biopolymer chains of the gelatin to the negatively charged exterior of the silicate nanoparticles. The 25-30 nm wide synthetic silicate nanoplatelets have been shown to have the capability to support the body's own healing factors and as a result accelerate the repair of damaged tissue [15].

This current study evaluated the potential of an osteogenic *in situ* gelling hydrogels with vascular patterns to be used for the treatment of bone defects. The STB composed of silicate nanoplatelets, gelatin, cells and VEGF loaded encapsulated PCL particles, which can

(a) be injected upon application of minimal strain
(b) solidify after injection force is removed
(c) and support growth and proliferation of cells

4.1 The shear-thinning gel for *in vitro* cultivation of cells

Silicate nanoplatelets have been shown to be cytocompatible and can promote the differentiation of stem cells in the absence of any osteoinductive factors [90]. Both gelatin and silicate nanoplatelets are highly biocompatible and can degrade into nontoxic components in physiological conditions [97] and are biocompatible with human cells [90, 98]. The STBs demonstrated good cell viability in both osteoblast cells and endothelial cells (see *Figure 24* - *Figure 31*). However, it was noted that in some cases the proliferation of cells

decreased over time, especially of osteoblast cells. To evaluate the underlying mechanisms that cause this proliferation decrease, further tests should be performed. The tests could be repeated with other cell types, such as pre-osteoblasts to evaluate the osteogenic differentiation of cells in STB.

Size of the PCL particles were influenced by the ultrasonication amplitude and exposure time. Higher amplitudes and longer exposure times lead to the formation of smaller particles. The incorporation of the biodegradable PCL polymer microbeads in the STB, lead to better cell viability of co-cultured cells and endothelial cells (see *Figure 31*). There was increased cell viability observed in the gels even after 7 days of culture. With the describe method, it is possible to make PCL particles with defined shape and size, depending on the release rate one desires to achieve. The cell tracker experiment could show that the cells survived in the scaffold even after 21 days of culture. The co-culture of the two cell types showed higher viability than the mono-culture of the cells. This proves that the osteoblast and endothelial cells have a synergistic relationship and support each other's growth [99, 100]. The encapsulation of VEGF within the PCL particles delivers a platform as carrier to store and release osteogenic and vascular growth factors for longer times, while improving the mechanical strength of STB. It was also shown that the total solid concentration of the silicate greatly influences the stiffness of STB. By controlling the silicate concentration, the mechanical properties of the gel can be fine-tuned to match the desired application.

4.2 Future perspectives

Hydrogel-based STB implants can protect its encapsulated cells by acting as a physical barrier between the cells and the immune system of the patient. As an additional advantage, the gel can be made very cost effectively and is cheaper than most bone implant materials. The goal of this project is to develop an innovative vascularized bone implant that can be injected into any shape or any size of the defect site. This will bring a breakthrough in medical treatment for non-union defect. For future applications, the bioprinting device could be used to effectively build 3D osteogenic hydrogel scaffolds with vascular patterns (see Figure 14). The user friendly and simplified functioning of this bioprinter would allow, inexperienced users to operate it with ease. This bioprinting device is also easy to use for *in situ* gelling during the surgery, without the need of generating heat. Based on this continuous multi-material extrusion platform, it would be possible to generate cell-laden patterns and complex 3D structures for various biomedical applications [94, 101].

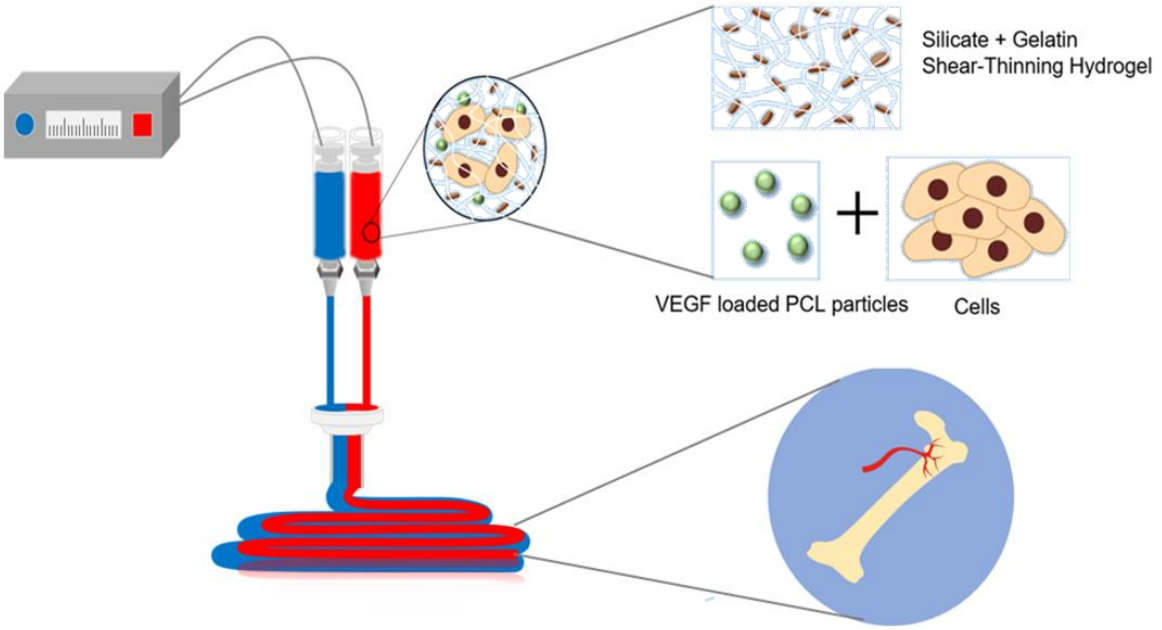

Figure 37: Schematic illustration of 3D-printed shear thinning hydrogel for bone repair (image made using PowerPoint).

Mouse osteoblast cells will be encapsulated within the bone part of the scaffold and mouse endothelial cells will be encapsulated in the vessel part of the scaffold. The scaffold could present a promising tissue engineered osteogenic *in situ* gelling hydrogel with vasculogenic patterns that could be used to make vascularized bone scaffolds of any shape or size.

4.3 Conclusion

Bone is a tissue with excellent regenerative ability [70]. This potential can be highly improved by vascularization of bone constructs. Although the vascular peripheral system in bone grafts can significantly improve osteogenesis and tissue integration, the formation of capillary vessel structures in bone graft requires extensive *in vitro* tissue cultures before this implant type can be applied to the clinic. In this respect, there is a need to develop microchannel structured bone implants that can allow blood perfusion throughout the construct and then further diffuse into capillary vessels to mimic the hierarchically structured blood vessels in human bone [9, 38, 102]. Thus, the combination of a bone and vessel cells and osteogenesis inducing matrix, such as STB and vascular growth factors within tissue engineered bone constructs can help repair larger bone defects more rapidly and will allow easier translation of research results into the clinical application and should be exploited more. The engineered osteogenic *in situ* gelling hydrogels with vasculogenic patterns could aid in overcoming critical barriers in developing a shape-tunable vascularized bone scaffold.

Bibliography

[1] O. Faour, R. Dimitriou, C. A. Cousins, and P. V. Giannoudis, "The use of bone graft substitutes in large cancellous voids: Any specific needs?," *Injury,* vol. 42, pp. S87-S90, 2011.

[2] V. Campana *et al.*, "Bone substitutes in orthopaedic surgery: From basic science to clinical practice," *Journal of Materials Science. Materials in Medicine,* vol. 25, no. 10, pp. 2445-61, 2014.

[3] T. A. Einhorn, "Enhancement of fracture-healing," *The Journal of Bone & Joint Surgery,* vol. 77, no. 6, pp. 940-56, 1995.

[4] S. Kumar, C. Wan, G. Ramaswamy, T. L. Clemens, and S. Ponnazhagan, "Mesenchymal stem cells expressing osteogenic and angiogenic factors synergistically enhance bone formation in a mouse model of segmental bone defect," *Molecular Therapy,* vol. 18, no. 5, pp. 1026-34, 2010.

[5] K. Fong *et al.*, "Predictors of nonunion and reoperation in patients with fractures of the tibia: An observational study," *BMC musculoskeletal disorders,* vol. 14, no. 1, p. 103, 2013.

[6] J. D. Heckman and J. Sarasohn-Kahn, "The economics of treating tibia fractures," *Bulletin Hospital for Joint Diseases,* vol. 56, no. 1, pp. 63-72, 1997.

[7] T. A. Einhorn, "Enhancement of fracture-healing," *JBJS,* vol. 77, no. 6, pp. 940-56, 1995.

[8] C. Meisinger, M. Wildner, J. Stieber, M. Heier, O. Sangha, and A. Döring, "Epidemiology of limb fractures," *Orthopade,* vol. 31, no. 1, pp. 92-9, 2002.

[9] S. Verrier *et al.*, "Tissue engineering and regenerative approaches to improving the healing of large bone defects," *Eur Cells Mater,* 2016.

[10] R. Marsell and T. A. Einhorn, "The biology of fracture healing," *Injury,* vol. 42, no. 6, pp. 551-5, 2011.

[11] A. Das, C. E. Segar, B. B. Hughley, D. T. Bowers, and E. A. Botchwey, "The promotion of mandibular defect healing by the targeting of s1p receptors and the recruitment of alternatively activated macrophages," *Biomaterials,* vol. 34, no. 38, pp. 9853-62, 2013.

[12] M. M. Stevens, "Biomaterials for bone tissue engineering," *Materials today,* vol. 11, no. 5, pp. 18-25, 2008.

[13] D. H. Copp and S. S. Shim, "The homeostatic function of bone as a mineral reservoir," *Oral Surgery, Oral Medicine, Oral Pathology,* vol. 16, no. 6, pp. 738-44, 1963.

[14] W. Schlickewei and C. Schlickewei, "The use of bone substitutes in the treatment of bone defects–the clinical view and history," *Macromolecular Sym.,* vol. 253, pp. 10-23, 2007.

[15] R. J. Miron and Y. F. Zhang, "Osteoinduction a review of old concepts with new standards," *Journal of dental research,* vol. 91, no. 8, pp. 736-44, 2012.

[16] T. A. Einhorn and L. C. Gerstenfeld, "Fracture healing: Mechanisms and interventions," *Nature Reviews Rheumatology,* vol. 11, no. 1, pp. 45-54, 2015.

[17] M. Brinker and D. O'Connor, "Nonunions: Evaluation and treatment," *Skeletal Trauma: Basic Science, Management, and Reconstruction. Browner BD, Levine AM, Jupiter JB, et al, eds. Philadelphia: WB Saunders,* pp. 507-604, 2003.

[18] S. Kadiyala, N. Jaiswal, and S. P. Bruder, "Culture-expanded, bone marrow-derived mesenchymal stem cells can regenerate a critical-sized segmental bone defect," *Tissue engineering,* vol. 3, no. 2, pp. 173-85, 1997.

[19] U. H. Lerner, "Neuropeptidergic regulation of bone resorption and bone formation," *Journal of Musculoskeletal and Neuronal Interactions,* vol. 2, no. 5, pp. 440-7, 2002.

[20] A. Togari, "Adrenergic regulation of bone metabolism: Possible involvement of sympathetic innervation of osteoblastic and osteoclastic cells," *Microscopy research and technique,* vol. 58, no. 2, pp. 77-84, 2002.

[21] C. Chenu, "Role of innervation in the control of bone remodeling," *Journal of Musculoskeletal and Neuronal Interactions,* vol. 4, no. 2, p. 132, 2004.

[22] Y. Zhang *et al.*, "Implant-derived magnesium induces local neuronal production of cgrp to improve bone-fracture healing in rats," *Nature Medicine,* vol. 22, no. 10, pp. 1160-9, 2016.

[23] T. Fukuda *et al.*, "Sema3a regulates bone-mass accrual through sensory innervations," *Nature,* vol. 497, no. 7450, pp. 490-3, 2013.

[24] M.-H. Lafage-Proust *et al.*, "Assessment of bone vascularization and its role in bone remodeling," *BoneKEy reports,* vol. 4, 2015.

[25] A. E. Mercado-Pagan, A. M. Stahl, Y. Shanjani, and Y. Yang, "Vascularization in bone tissue engineering constructs," (in eng), *Ann Biomed Eng,* vol. 43, no. 3, pp. 718-29, 2015.

[26] A. R. Amini, C. T. Laurencin, and S. P. Nukavarapu, "Bone tissue engineering: Recent advances and challenges," (in eng), *Crit Rev Biomed Eng,* vol. 40, no. 5, pp. 363-408, 2012.

[27] L. H. Nguyen *et al.*, "Vascularized bone tissue engineering: Approaches for potential improvement," (in eng), *Tissue Eng Part B Rev,* vol. 18, no. 5, pp. 363-82, 2012.

[28] P. Carmeliet, "Angiogenesis in health and disease," *Nature Medicine,* vol. 9, no. 6, p. 653, 2003.

[29] D. M. Findlay and D. R. Haynes, "Mechanisms of bone loss in rheumatoid arthritis," *Modern rheumatology,* vol. 15, no. 4, pp. 232-40, 2005.

[30] S. Aharinejad *et al.*, "Microvascular pattern in the metaphysis during bone growth," *Anat Rec,* vol. 242, no. 1, pp. 111-22, 1995.

[31] D. A. Walsh and P. I. Mapp, "Joint physiology and synovial cell proliferation," *Rheumatology,* vol. 37, no. 9, pp. 1032-3, 1998.

[32] R. S. Taichman, C. Cooper, E. T. Keller, K. J. Pienta, N. S. Taichman, and L. K. McCauley, "Use of the stromal cell-derived factor-1/cxcr4 pathway in prostate cancer metastasis to bone," *Cancer research,* vol. 62, no. 6, pp. 1832-7, 2002.

[33] E. Polykandriotis, A. Arkudas, R. E. Horch, M. Stürzl, and U. Kneser, "Autonomously vascularized cellular constructs in tissue engineering: Opening a new perspective for biomedical science," *J Cell Mol Med,* vol. 11, no. 1, pp. 6-20, 2007.

[34] U. Kneser, D. J. Schaefer, E. Polykandriotis, and R. E. Horch, "Tissue engineering of bone: The reconstructive surgeon's point of view," *J Cell Mol Med,* vol. 10, no. 1, pp. 7-19, 2006.

[35] J.-j. Fan, T.-w. Mu, J.-j. Qin, L. Bi, and G.-x. Pei, "Different effects of implanting sensory nerve or blood vessel on the vascularization, neurotization, and osteogenesis of tissue-engineered bone in vivo," *Biomed Res Int,* vol. 2014, 2014.

[36] R. El-Gendy, J. Kirkham, P. J. Newby, Y. Mohanram, A. R. Boccaccini, and X. B. Yang, "Investigating the vascularization of tissue-engineered bone constructs using dental pulp cells and 45s5 bioglass(®) scaffolds," *Tissue Eng Part A,* vol. 21, no. 13-14, pp. 2034-43, 2015.

[37] B. Clarke, "Normal bone anatomy and physiology," *Clinical journal of the American Society of Nephrology,* vol. 3, no. Supplement 3, pp. S131-S9, 2008.

[38] J. Trueta, "The role of the vessels in osteogenesis," *Bone & Joint Journal,* vol. 45, no. 2, pp. 402-18, 1963.

[39] K. Draenert and Y. Draenert, "The vascular system of bone marrow," *Scanning electron microscopy,* no. 4, pp. 113-22, 1979.

[40] M. Laroche, "Intraosseous circulation from physiology to disease," *Joint Bone Spine,* vol. 69, no. 3, pp. 262-9, 2002.

[41] E. O. Johnson, K. Soultanis, and P. N. Soucacos, "Vascular anatomy and microcirculation of skeletal zones vulnerable to osteonecrosis: Vascularization of the femoral head," *Orthopedic Clinics of North America,* vol. 35, no. 3, pp. 285-91, 2004.

[42] A. Wilson and A. Trumpp, "Bone-marrow haematopoietic-stem-cell niches," *Nature Reviews Immunology,* vol. 6, no. 2, pp. 93-106, 2006.

[43] A. P. Kusumbe, S. K. Ramasamy, and R. H. Adams, "Coupling of angiogenesis and osteogenesis by a specific vessel subtype in bone," *Nature,* vol. 507, no. 7492, pp. 323-8, 2014.

[44] T. Takarada *et al.*, "Genetic analysis of runx2 function during intramembranous ossification," *Development,* vol. 143, no. 2, pp. 211-8, 2016.

[45] N. Ortega, D. J. Behonick, and Z. Werb, "Matrix remodeling during endochondral ossification," *Trends in cell biology,* vol. 14, no. 2, pp. 86-93, 2004.

[46] B. K. Hall and T. Miyake, "The membranous skeleton: The role of cell condensations in vertebrate skeletogenesis," *Anatomy and embryology,* vol. 186, no. 2, pp. 107-24, 1992.

[47] J. M. Kanczler and R. O. Oreffo, "Osteogenesis and angiogenesis: The potential for engineering bone," *Eur Cell Mater,* vol. 15, no. 2, pp. 100-14, 2008.

[48] H.-P. Gerber and N. Ferrara, "Angiogenesis and bone growth," *Trends in cardiovascular medicine,* vol. 10, no. 5, pp. 223-8, 2000.

[49] B. K. Hall and T. Miyake, "All for one and one for all: Condensations and the initiation of skeletal development," *Bioessays,* vol. 22, no. 2, pp. 138-47, 2000.

[50] P. Collin-Osdoby, "Role of vascular endothelial cells in bone biology," *Journal of cellular biochemistry,* vol. 55, no. 3, pp. 304-9, 1994.

[51] G. Bluteau *et al.*, "Vegf and vegf receptors are differentially expressed in chondrocytes," *Bone,* vol. 40, no. 3, pp. 568-76, 2007.

[52] W. Petersen, T. Pufe, B. Kurz, R. Mentlein, and B. Tillmann, "Angiogenesis in fetal tendon development: Spatial and temporal expression of the angiogenic peptide vascular endothelial cell growth factor," *Anatomy and embryology,* vol. 205, no. 4, pp. 263-70, 2002.

[53] V. Midy and J. Plouét, "Vasculotropin/vascular endothelial growth factor induces differentiation in cultured osteoblasts," *Biochemical and biophysical research communications,* vol. 199, no. 1, pp. 380-6, 1994.

[54] M. M. L. Deckers, M. Karperien, C. van der Bent, T. Yamashita, S. E. Papapoulos, and C. W. G. M. Löwik, "Expression of vascular endothelial growth factors and their receptors during osteoblast differentiation," *Endocrinology,* vol. 141, no. 5, pp. 1667-74, 2000.

[55] M. T. Engsig *et al.*, "Matrix metalloproteinase 9 and vascular endothelial growth factor are essential for osteoclast recruitment into developing long bones," *The Journal of cell biology,* vol. 151, no. 4, pp. 879-90, 2000.

[56] R. H. Yabsley and W. R. Harris, "The effect of shaft fractures and periosteal stripping on the vascular supply to epiphyseal plates," *Jbjs,* vol. 47, no. 3, pp. 551-66, 1965.

[57] T. Tammela, B. Enholm, K. Alitalo, and K. Paavonen, "The biology of vascular endothelial growth factors," *Cardiovascular research,* vol. 65, no. 3, pp. 550-63, 2005.

[58] B. M. Roux, M. H. Cheng, and E. M. Brey, "Engineering clinically relevant volumes of vascularized bone," *J Cell Mol Med,* vol. 19, no. 5, pp. 903-14, 2015.

[59] K. D. Hankenson, M. Dishowitz, C. Gray, and M. Schenker, "Angiogenesis in bone regeneration," *Injury,* vol. 42, no. 6, pp. 556-61, 2011.

[60] K. Dickson, S. Katzman, E. Delgado, and D. Contreras, "Delayed unions and nonunions of open tibial fractures: Correlation with arteriography results," *Clinical orthopaedics and related research,* vol. 302, pp. 189-93, 1994.

[61] J. Glowacki, "Angiogenesis in fracture repair," *Clinical orthopaedics and related research,* vol. 355, pp. S82-S9, 1998.

[62] J. Street *et al.*, "Vascular endothelial growth factor stimulates bone repair by promoting angiogenesis and bone turnover," *Proceedings of the National Academy of Sciences,* vol. 99, no. 15, pp. 9656-61, 2002.

[63] M. Raida, A. C. Heymann, C. Günther, and D. Niederwieser, "Role of bone morphogenetic protein 2 in the crosstalk between endothelial progenitor cells and mesenchymal stem cells," *Bone,* vol. 16, p. 17, 2006.

[64] R. E. Horch, J. P. Beier, U. Kneser, and A. Arkudas, "Successful human long-term application of in situ bone tissue engineering," (in eng), *J Cell Mol Med,* vol. 18, no. 7, pp. 1478-85, 2014.

[65] T. J. Blokhuis, G. M. Calori, and G. Schmidmaier, "Autograft versus bmps for the treatment of non-unions: What is the evidence?," *Injury,* vol. 44, pp. S40-S2, 2013.

[66] J. B. Moore, J. M. Mazur, D. Zehr, P. K. Davis, E. G. Zook, and J. B. Moon, "A biomechanical comparison of vascularized and conventional autogenous bone grafts," *Plast Reconstr Surg,* vol. 73, no. 3, pp. 382-6, 1984.

[67] M. K. Sen and T. Miclau, "Autologous iliac crest bone graft: Should it still be the gold standard for treating nonunions?," *Injury,* vol. 38, no. 1, pp. S75-S80, 2007.

[68] J. Baumhauer, M. S. Pinzur, R. Donahue, W. Beasley, and C. DiGiovanni, "Site selection and pain outcome after autologous bone graft harvest," *Foot & ankle international,* vol. 35, no. 2, pp. 104-7, 2014.

[69] D. M. Ehrler and A. R. Vaccaro, "The use of allograft bone in lumbar spine surgery," (in eng), *Clin Orthop Relat Res,* no. 371, pp. 38-45, 2000.

[70] M. Frohlich, W. L. Grayson, L. Q. Wan, D. Marolt, M. Drobnic, and G. Vunjak-Novakovic, "Tissue engineered bone grafts: Biological requirements, tissue culture and clinical relevance," (in eng), *Curr Stem Cell Res Ther,* vol. 3, no. 4, pp. 254-64, 2008.

[71] K. B. Jones, A. V. Mollano, J. A. Morcuende, R. R. Cooper, and C. L. Saltzman, "Bone and brain: A review of neural, hormonal, and musculoskeletal connections," (in eng), *Iowa Orthop J,* vol. 24, pp. 123-32, 2004.

[72] J. Fan *et al.*, "Microsurgical techniques used to construct the vascularized and neurotized tissue engineered bone," (in eng), *Biomed Res Int,* vol. 2014, p. 281872, 2014.

[73] L. Feng, E. Lingling, and H. Liu, "The effects of separating inferior alveolar neurovascular bundles on osteogenesis of tissue-engineered bone and vascularization," (in eng), *Biomed Pap Med Fac Univ Palacky Olomouc Czech Repub,* vol. 159, no. 4, pp. 637-41, 2015.

[74] S. Y. Chen *et al.*, "Different effects of implanting vascular bundles and sensory nerve tracts on the expression of neuropeptide receptors in tissue-engineered bone in vivo," (in eng), *Biomed Mater,* vol. 5, no. 5, p. 055002, 2010.

[75] A. Weigand *et al.*, "Acceleration of vascularized bone tissue-engineered constructs in a large animal model combining intrinsic and extrinsic vascularization," (in eng), *Tissue Eng Part A,* vol. 21, no. 9-10, pp. 1680-94, 2015.

[76] S. Chen *et al.*, "[effect of tissue engineered bone implantation with vascular bundle and sensory nerve bundle on expression of neurokinin 1 receptor and vasoactive intestinal peptide type 1 receptor in vivo]," (in chi), *Zhongguo Xiu Fu Chong Jian Wai Ke Za Zhi,* vol. 24, no. 7, pp. 785-91, 2010.

[77] S. K. Ramasamy, A. P. Kusumbe, L. Wang, and R. H. Adams, "Endothelial notch activity promotes angiogenesis and osteogenesis in bone," *Nature,* vol. 507, no. 7492, pp. 376-80, 2014.

[78] Y. Kang, N. Mochizuki, A. Khademhosseini, J. Fukuda, and Y. Yang, "Engineering a vascularized collagen-β-tricalcium phosphate graft using an electrochemical approach," *Acta biomaterialia,* vol. 11, pp. 449-58, 2015.

[79] J. Wang *et al.*, "In vitro osteogenesis of human adipose-derived stem cells by coculture with human umbilical vein endothelial cells," *Biochemical and biophysical research communications,* vol. 412, no. 1, pp. 143-9, 2011.

[80] C. Maes *et al.*, "Increased skeletal vegf enhances β-catenin activity and results in excessively ossified bones," *The EMBO Journal,* vol. 29, no. 2, pp. 424-41, 2010.

[81] P. Lips, P. Courpron, and P. Meunier, "Mean wall thickness of trabecular bone packets in the human iliac crest: Changes with age," *Calcified tissue research,* vol. 26, no. 1, pp. 13-7, 1978.

[82] D. Smith, M. Khairi, and C. Johnston Jr, "The loss of bone mineral with aging and its relationship to risk of fracture," *Journal of clinical investigation,* vol. 56, no. 2, p. 311, 1975.

[83] W. Bian and N. Bursac, "Tissue engineering of functional skeletal muscle: Challenges and recent advances," (in eng), *IEEE Eng Med Biol Mag,* vol. 27, no. 5, pp. 109-13, 2008.

[84] A. K. Gaharwar *et al.*, "Shear-thinning nanocomposite hydrogels for the treatment of hemorrhage," *ACS Nano,* vol. 8, no. 10, pp. 9833-42, 2014.

[85] J. R. Xavier *et al.*, "Bioactive nanoengineered hydrogels for bone tissue engineering: A growth-factor-free approach," *ACS Nano,* vol. 9, no. 3, pp. 3109-18, 2015.
[86] C. Yan, A. Altunbas, T. Yucel, R. P. Nagarkar, J. P. Schneider, and D. J. Pochan, "Injectable solid hydrogel: Mechanism of shear-thinning and immediate recovery of injectable β-hairpin peptide hydrogels," (in eng), *Soft Matter,* vol. 6, no. 20, pp. 5143-56, 2010.
[87] C. W. Macosko, *Rheology: Principles, measurements, and applications*. VCH 1994.
[88] D. Xu and C. Y. Liu, "Divergent shear thinning and shear thickening behavior of supramolecular polymer networks in semidilute entangled polymer solutions," (in eng), vol. 44, no. 7, pp. 2343-53, 2011.
[89] S. Haavisto, A. I. Koponen, and J. Salmela, "New insight into rheology and flow properties of complex fluids with doppler optical coherence tomography," (in eng), *Front Chem,* vol. 2, 2014.
[90] A. K. Gaharwar *et al.*, "Bioactive silicate nanoplatelets for osteogenic differentiation of human mesenchymal stem cells," *Advanced materials,* vol. 25, no. 24, pp. 3329-36, 2013.
[91] !!! INVALID CITATION !!! {}.
[92] A. K. Gaharwar *et al.*, "Physically crosslinked nanocomposites from silicate-crosslinked peo: Mechanical properties and osteogenic differentiation of human mesenchymal stem cells," (in eng), *Macromol Biosci,* vol. 12, no. 6, pp. 779-93, 2012.
[93] U. Bilati, E. Allemann, and E. Doelker, "Sonication parameters for the preparation of biodegradable nanocapsules of controlled size by the double emulsion method," (in eng), *Pharm Dev Technol,* vol. 8, no. 1, pp. 1-9, 2003.
[94] W. Liu *et al.*, "Rapid continuous multimaterial extrusion bioprinting," (in eng), *Adv Mater,* vol. 29, no. 3, 2017.
[95] R. K. Avery *et al.*, "An injectable shear-thinning biomaterial for endovascular embolization," *Science Translational Medicine,* vol. 8, no. 365, pp. 365ra156-365ra156, 2016.
[96] S. Neri, E. Mariani, A. Meneghetti, L. Cattini, and A. Facchini, "Calcein-acetyoxymethyl cytotoxicity assay: Standardization of a method allowing additional analyses on recovered effector cells and supernatants," (in eng), *Clin Diagn Lab Immunol,* vol. 8, no. 6, pp. 1131-5, 2001.
[97] D. W. Thompson and J. T. Butterworth, "The nature of laponite and its aqueous dispersions," *Journal of Colloid and Interface Science,* vol. 151, no. 1, pp. 236-43, 1992.
[98] A. K. Gaharwar *et al.*, "Physically crosslinked nanocomposites from silicate-crosslinked peo: Mechanical properties and osteogenic differentiation of human mesenchymal stem cells," *Macromol Biosci,* vol. 12, no. 6, pp. 779-93, 2012.
[99] Y.-Q. Yang, Y.-Y. Tan, R. Wong, A. Wenden, L.-K. Zhang, and A. B. M. Rabie, "The role of vascular endothelial growth factor in ossification," *In J Oral Sci,* vol. 4, no. 2, pp. 64-8, 2012.
[100] J. Street *et al.*, "Vascular endothelial growth factor stimulates bone repair by promoting angiogenesis and bone turnover," *Proceedings of the National Academy of Sciences of the United States of America,* vol. 99, no. 15, pp. 9656-61, 2002.
[101] W. Liu *et al.*, "Rapid continuous multimaterial extrusion bioprinting," *Advanced materials,* 2016.

[102] A. J. Salgado *et al.*, "Tissue engineering and regenerative medicine: Past, present, and future," (in eng), *Int Rev Neurobiol,* vol. 108, pp. 1-33, 2013.

List of Figures

List of Tables

List of Abbreviations

Ang-1	Angiopoietin-1
BMP-2	Bone morphogenetic protein-2
CD31	Cluster of Differentiation 31
Cx43	Connexin 43
PBS	Dulbecco’s phosphate-buffered saline
EDTA	Trypsin-ethylenediaminetetraacetic acid
FBS	Fetal bovine serum
FGF	Fibroblast growth factor
FITC-Dextran	Fluorescein isothiocyanate–dextrantran
G'	Storage Modulus
HDPSCs	Human dental pulp stromal cells
HUVECs	Human umbilical vein endothelial cells
IGF-1	Insulin-like growth factor-1
MMP 13	Matrix metalloprotease 13
MSCs	Mesenchymal stem cells
NK1R	Neurokinin 1 receptor
Pa	Pascals
PCL	Polycaprolactone
PDGF	Platelet- derived growth factor
PDMS	Polydimethylsiloxane
PVA	Polyvinyl Alcohol
RPM	Revolutions per minute
SEM	Scanning electron microscope
STB	Shear-thinning biomaterial
VEGF	Vascular endothelial growth factor
VEGFR1	Tyrosine kinase receptors flt-1
VIPR1	Vasoactive intestinal peptide type 1 receptor
W-O-W	Water in Mineral Oil in Water

Appendix

Reagents and Equipment

Name	Cat. No.	Company
Aqueous Ethanol 70%	ERM-AC407	ZAG Chemistry, USA
BD Precisionglide® Syringe Needles Gauge 18, L 1 In.	Z192554	Sigma-Aldrich, St. Louis, MO
BSA	A2058	Sigma Aldrich, St. Louis, USA
Cell Culture Dishes	430589, 430578, 438023	Fisher Scientific, USA
Cell Culture Medium DMEM	P04-01548	PAN Biotech, Country
Complete Mouse Endothelial Cell Medium	M1168	Cell Biologics, USA
DAPI	D9542	Sigma-Aldrich, St. Louis, MO
Dichloromethane	57648216	DCM, Acros Organics, Pittsburg, PA
PBS	14190	Gibco, USA
Falcon Tubes	352096	BD Biosciences, USA
FBS	10437-028	Gibco, Life Technologies, Grand Island, NY, USA
FBS	26140	Gibco, USA
FESEM	Ultra 55	Zeiss, Germany
FITC-Dextran Molecules	60842-46-8	Sigma Aldrich, St. Louis, USA
Fluorescent Colors	5201, 5204, 5408	Createx Colors, USA
Fluorescence Microscope	Axio Observer D1	Zeiss, Germany
Green CMFDA Cell Tracker	C2925	Molecular Probes, Invitrogen, Canada
Live/Dead Dyes: Calcein AM and Ethidium Homodimer-1	L3224	Molecular Probes, USA
Mechanical Tester	Instron Model 5542	Instruments, DE, USA
Mineral Oil	P-5927	CVS Pharmacy
Mouse Osteoblasts	MC3T3-E1	Sigma, USA
Needles	18-Gauge	BD Biosciences
PCL	440744	Sigma-Aldrich, USA

PDMS	184 Silicon Elastomer Kit	Dow Corning Sylgard, USA
Phosphate Buffered Saline (PBS)	SH3025601	Hyclone, Thermo Scientific (Logan, UT, USA)
Pipetman	P200, #69989-5	Gilson, Country
Pipette Tips 20-1000 Ul	3120000917	Eppendorf, Country
Primary Mammary Microvascular Endothelial Cells	BALB-5020	Cell Biologics, USA
Qsonica Sonicator	#Q500	Newton, CT, USA
Red CMTPX Cell Tracker	C34552	Molecular Probes, Invitrogen, Canada
Rheometer	ARES-G2	TA Instruments, DE, USA
Sterile Hamilton Syringe, 100 Ul SYR	84884	Hamilton, Country
Sterile Syringe, BD 10 Ml	300912	BD. Sigma-Aldrich, St. Louis, MO
Synthetic silicate nanoplatelets	Laponite XLG	Southern Clay Products, Inc., Louisville, KY
Trypsin-EDTA	15400	Gibco, USA
Triton™ X-100	9002-93-1	Sigma-Aldrich, St. Louis, MO
Type-A porcine skin gelatin	G2500-100G	Sigma-Aldrich; Milwaukee, WI
VEGF	100-20	Peprotech, USA